JHEP

Published for SISSA by Springer

Received: October 11, 2018
Revised: January 8, 2019
Accepted: January 30, 2019
Published: February 5, 2019

Loop corrections to dark matter direct detection in a pseudoscalar mediator dark matter model

Tomohiro Abe,[a,b] **Motoko Fujiwara**[c] **and Junji Hisano**[b,c,d]

[a] *Institute for Advanced Research, Nagoya University, Furo-cho Chikusa-ku, Nagoya, Aichi, 464-8602 Japan*
[b] *Kobayashi-Maskawa Institute for the Origin of Particles and the Universe, Nagoya University, Furo-cho Chikusa-ku, Nagoya, Aichi, 464-8602 Japan*
[c] *Department of Physics, Nagoya University, Furo-cho Chikusa-ku, Nagoya, Aichi, 464-8602 Japan*
[d] *Kavli IPMU (WPI), UTIAS, University of Tokyo, Kashiwa, Chiba 277-8584, Japan*

E-mail: abetomo@kmi.nagoya-u.ac.jp, motoko@eken.phys.nagoya-u.ac.jp, hisano@eken.phys.nagoya-u.ac.jp

Abstract: If dark matter (DM) is a fermion and its interactions with the standard model particles are mediated by pseudoscalar particles, the tree-level amplitude for the DM-nucleon elastic scattering is suppressed by the momentum transfer in the non-relativistic limit. At the loop level, on the other hand, the spin-independent contribution to the cross section appears without such suppression. Thus, the loop corrections are essential to discuss the sensitivities of the direct detection experiments for the model prediction. The one-loop corrections were investigated in the previous works. However, the two-loop diagrams give the leading order contribution to the DM-gluon effective operator ($\bar{\chi}\chi G^a_{\mu\nu}G^{a\mu\nu}$) and have not been correctly evaluated yet. Moreover, some interaction terms which affect the scattering cross section were overlooked. In this paper, we show the cross section obtained by the improved analysis and discuss the region where the cross section becomes large.

Keywords: Beyond Standard Model, Cosmology of Theories beyond the SM, Effective Field Theories

ArXiv ePrint: 1810.01039

https://doi.org/10.1007/JHEP02(2019)028

JHEP02(2019)028

Contents

JHEP02(2019)028

1 Introduction

Weakly Interacting Massive Particles (WIMPs) are popular dark matter (DM) candidates and often appear in models beyond the standard model (BSM). A variety of models have been studied in the literature. They typically predict scattering processes between DM and nucleon with a sizable cross section which can be detected experimentally. There are many DM direct detection experiments such as the LUX [1], PandaX-II [2], and XENON1T experiments [3]. The significant DM signals have not been reported yet, and these experiments give severe upper bounds on the DM-nucleon spin-independent (SI) scattering cross

section ($\sigma_{\rm SI}$). This fact gives a strong constraint for the parameter space of the models which predict a WIMP as a DM candidate.

A pseudoscalar coupling with fermion DM is a simple way to avoid these strong constraints from the DM direct detection experiments [4, 5],

$$\bar{\chi} i\gamma^5 \chi s, \tag{1.1}$$

where χ is a fermion as a DM candidate and s is a scalar mediator connecting the DM and the standard model (SM) sector. In the non-relativistic limit, this interaction term predicts the suppression of the tree-level DM-nucleon scattering amplitude by the momentum transfer. On the other hand, the amplitude for DM annihilation processes is predicted as s-wave. Therefore the interaction term in eq. (1.1) has desirable features for WIMP models, namely models can evade the strong constraints from the DM direct detection experiments while keeping the annihilation cross section to explain the amount of the DM in our universe as a thermal relic abundance.

A pseudoscalar mediator model [6] is one of the simplest models which predict the interaction term in eq. (1.1), and its phenomenology has been widely studied [7–14]. In the model, χ is a gauge singlet fermion, and s is a gauge singlet pseudoscalar. The Higgs sector is extended into the two-Higgs doublet models (THDMs) to make the gauge singlet pseudoscalar interact with the SM sector at the renormalizable level. CP invariance is assumed in the DM and the mediator sectors.[1]

In this model, $\sigma_{\rm SI}$ is generated at the loop level [6, 11, 13, 14]. Although $\sigma_{\rm SI}$ is suppressed by the loop factors and is smaller than the current upper bounds from the direct detection experiments, it can be larger than the neutrino floor [19] and can be detected by the future DM direct detection experiments. Therefore it is essential to evaluate the cross section at the loop level. However, $\sigma_{\rm SI}$ has been calculated without including some relevant interaction terms in [6, 11, 13, 14]. Moreover, two-loop diagrams which induce the DM-gluon effective operator, $\bar{\chi}\chi G^a_{\mu\nu} G^{a\mu\nu}$, have not been correctly calculated as was mentioned in [11].

In this paper, we give a complete set for the leading order calculations in the pseudoscalar mediator DM model.[2] We take into account all of the renormalizable interaction terms. We find that quartic interaction terms between the pseudoscalar and the SM Higgs bosons, which have been ignored in [6, 11], are important to enhance $\sigma_{\rm SI}$. As a result of the enhancement, the model can be detected by the XENONnT [20], LZ [21], and DARWIN experiments [22] in some parameter regions. We also calculate the relevant two-loop diagrams for the DM-gluon effective operators. In [11], the contribution was estimated from the one-loop box diagrams by using a relation between a heavy quark scalar-type operator and a gluon scalar-type operator [23] without justification. We find that the contributions from the charm and bottom quarks were underestimated, while the contribution from the

[1] If the DM and/or the mediator sector breaks the CP invariance, the mediator can have renormalizable interactions with the SM sector without extending the Higgs sector into the THDMs, see for example [15–18].

[2] χ is a Dirac fermion in [6, 11, 13, 14]. In this paper, however, we consider χ as a Majorana fermion to make the model much simpler. Qualitative features are the same both in the Dirac and the Majorana cases.

JHEP02(2019)028

top quark was overestimated in [11]. In the end, we clarify that the contribution from the box diagrams is subdominant and the triangle diagrams dominate the scattering process.

The structure of this paper is as follows: in section 2, we introduce the gauge invariant renormalizable model which contains the pseudoscalar mediators [6]. In section 3, we derive the effective operators which induce the DM-nucleon SI scattering. In section 4, we show our numerical results. We compare our result with the previous one in [11], and then search the parameter space where $\sigma_{\rm SI}$ becomes large enough to reach the prospects of the direct detection experiments. Our conclusions are in section 5. In appendix A, we show explicit formulas for scalar trilinear couplings which are defined in section 2. In appendix B, we write the details of the derivation of the effective operators for SI scattering between DM and quarks/gluon. In appendix C, we define the loop functions used in section 3.

2 Model

In this section, we briefly review the pseudoscalar mediator DM model [6]. The model contains a gauge singlet Majorana fermion χ as a DM candidate and a gauge singlet pseudoscalar boson a_0 as a mediator field. The DM can be expressed using Weyl spinor ψ as follows:

$$\chi = \begin{pmatrix} \psi \\ \psi^\dagger \end{pmatrix}. \tag{2.1}$$

The Higgs sector is also extended into a THDM, which contains two $\mathrm{SU}(2)_L$ doublet scalar fields H_j $(j = 1, 2)$ with a hypercharge $Y = 1/2$.

We assume a Z_2 symmetry to stabilize the DM candidate. Under this Z_2 symmetry, χ is odd, and all the other fields are even. The interaction terms of the DM and scalar fields are given by

$$\mathcal{L} \supset + i\frac{g_\chi}{2} a_0 \bar{\chi}\gamma^5\chi - (V_{\rm THDM} + V_{a_0} + V_{\rm port}), \tag{2.2}$$

where

$$\begin{aligned} V_{\rm THDM} = {} & m_1^2 H_1^\dagger H_1 + m_2^2 H_2^\dagger H_2 - m_3^2 \left(H_1^\dagger H_2 + \text{h.c.}\right) \\ & + \frac{\lambda_1}{2}(H_1^\dagger H_1)^2 + \frac{\lambda_2}{2}(H_2^\dagger H_2)^2 + \lambda_3 (H_1^\dagger H_1)(H_2^\dagger H_2) + \lambda_4 (H_1^\dagger H_2)(H_2^\dagger H_1) \\ & + \frac{\lambda_5}{2}\left[(H_1^\dagger H_2)^2 + \text{h.c.}\right], \end{aligned} \tag{2.3}$$

$$V_{a_0} = \frac{1}{2} m_{a_0}^2 a_0^2 + \frac{\lambda_{a_0}}{4} a_0^4, \tag{2.4}$$

$$V_{\rm port} = \kappa (i a_0 H_1^\dagger H_2 + \text{h.c.}) + c_1 a_0^2 H_1^\dagger H_1 + c_2 a_0^2 H_2^\dagger H_2. \tag{2.5}$$

Here we assume CP invariance in eq. (2.2), and therefore all the parameters in eq. (2.2) are real. We also assume a softly broken Z_4 symmetry to avoid flavor changing Higgs couplings at the tree-level. This symmetry is an extension of the softly broken Z_2 symmetry often

JHEP02(2019)028

	Q_L^i, L_L^i	u_R^i	d_R^i	e_R^i
Type-I	+	−	−	−
Type-II	+	−	+	+
Type-X	+	−	−	+
Type-Y	+	−	+	−

Table 1. The charge assignments of the Z_4 symmetry for the SM fermions, where Q_L^i, L_L^i, u_R^i, d_R^i, and e_R^i are the i-th generation of the left-handed quark, the left-handed lepton, the right-handed up-type quark, the right-handed down-type quark, and the right-handed charged lepton, respectively ($i = 1, 2, 3$).

assumed in studies of the THDMs [24–26] to avoid flavor changing scalar couplings [27].[3] Under this Z_4 symmetry, each field is transformed as follows:

$$\psi \mapsto i\psi, \tag{2.6}$$

$$a_0 \mapsto -a_0, \tag{2.7}$$

$$H_1 \mapsto H_1, \tag{2.8}$$

$$H_2 \mapsto -H_2. \tag{2.9}$$

For the SM fermions, there are four variations in charge assignments as summarized in table 1. This Z_4 symmetry is softly broken by the DM mass term as well as the m_3^2 term in $V_{\rm THDM}$.[4]

As can be seen from the scalar potential, a_0 is mixed with the CP-odd scalar in the THDM sector after the electroweak symmetry breaking, and thus the DM interacts with the SM particles by exchanging the pseudoscalar particles. This interaction structure is crucial to evade the direct detection constraints as we mentioned in the introduction.

Note that the interaction terms proportional to c_i ($i = 1, 2$) were not included in the analysis of [6] and [11]. Although the existence of these interaction terms was pointed out in [13], they also neglected these terms in their analysis. As we will see in later, however, the effect of the c_2 term plays an important role in a DM-nucleon scattering process for the DM direct detection experiments.

The field definitions of the Higgs doublets are as follows:

$$H_j = \begin{pmatrix} \phi_j^+ \\ \frac{1}{\sqrt{2}}(v_j + \rho_j + i\eta_j) \end{pmatrix} \quad (j = 1, 2), \tag{2.10}$$

where v_j is the vacuum expectation value of each doublet field. We introduce $\tan\beta$ as the ratio of v_1 and v_2,

$$\tan\beta = \frac{v_2}{v_1}, \qquad v^2 = v_1^2 + v_2^2, \tag{2.11}$$

[3] For the analysis without any discrete symmetry to forbid the flavor changing scalar couplings, see [28].

[4] This Z_4 symmetry is different from the Z_2 symmetry for the DM stability which we mentioned above.

JHEP02(2019)028

where $v \simeq 246$ GeV, the vacuum expectation value of the SM Higgs boson. For simplicity, we use t_β as an abbreviation for $\tan\beta$. We assume that a_0 has no vacuum expectation value. Then, the scalar mass eigenstates are given from the weak eigenstates as follows:

$$\begin{pmatrix} G^\pm \\ H^\pm \end{pmatrix} = \begin{pmatrix} \cos\beta & \sin\beta \\ -\sin\beta & \cos\beta \end{pmatrix} \begin{pmatrix} \phi_1^\pm \\ \phi_2^\pm \end{pmatrix}, \tag{2.12}$$

$$\begin{pmatrix} H \\ h \end{pmatrix} = \begin{pmatrix} \cos\alpha & \sin\alpha \\ -\sin\alpha & \cos\alpha \end{pmatrix} \begin{pmatrix} \rho_1 \\ \rho_2 \end{pmatrix}, \tag{2.13}$$

$$\begin{pmatrix} G_0 \\ A \\ a \end{pmatrix} = \begin{pmatrix} 1 & 0 & 0 \\ 0 & \cos\theta & \sin\theta \\ 0 & -\sin\theta & \cos\theta \end{pmatrix} \begin{pmatrix} \cos\beta & \sin\beta & 0 \\ -\sin\beta & \cos\beta & 0 \\ 0 & 0 & 1 \end{pmatrix} \begin{pmatrix} \eta_1 \\ \eta_2 \\ a_0 \end{pmatrix}, \tag{2.14}$$

where $G^\pm$ and G_0 are would-be Nambu Goldstone bosons for $W^\pm$ and Z, respectively. There is the following relation between θ and κ.[5]

$$\sin 2\theta = \frac{-2\kappa v}{m_A^2 - m_a^2}, \tag{2.15}$$

where m_a and m_A are the mass eigenvalues of the pseudoscalar states a and A, respectively.

In the following discussion, we take the alignment limit $\sin(\beta-\alpha) \to 1$ where arbitrary values of t_β are allowed from the latest LHC constraints [29, 30].[6] Under this limit, the interactions of h are similar to those of the SM-Higgs boson. We also assume $m_H = m_{H_\pm} = m_A$ to avoid constraints from the electroweak precision measurements by enhancing the custodial symmetry. Under this setup, the free parameters of this model are as follows:

$$\{m_\chi,\ g_\chi,\ m_a,\ m_A,\ \theta,\ t_\beta,\ c_1,\ c_2\}. \tag{2.16}$$

In the following, we briefly review the constraints on these parameters. In this paper, we focus on the parameter regions which are allowed for all the THDM types. The lower bound on the charged Higgs boson mass is $m_{H_\pm} > 580\,\text{GeV}$ from $B \to X_s\gamma$ for the type-II THDM [31], and thus we take $m_H = m_{H_\pm} = m_A = 600\,\text{GeV}$ as the benchmark point. With this choice, we find that $8 \lesssim t_\beta \lesssim 15$ [32, 33] and take $t_\beta = 10$ as the benchmark point. As for the light pseudoscalar mass, we find $m_a > m_h/2$ from the constraint on the Higgs branching ratio [29, 34] as discussed in section 4.3. Since the loop corrections to σ_{SI} is smaller for the larger m_a, we focus on $m_a \lesssim 100\,\text{GeV}$. We have checked that θ is not constrained with these parameters [9] and simply take the same value as in [11].

[5] Note that the overall sign disagrees with the expression shown in [6] and [11] when $\sin 2\theta$ is rearranged to be $\tan 2\theta$.

[6] A large difference of $\beta-\alpha$ from $\pi/2$ is disfavored. The measurements of the Higgs couplings give the most stringent bound on $\beta-\alpha$. For example, $|\cos(\beta-\alpha)| \lesssim 0.01$ is allowed for all the types of the THDM with $t_\beta = 10$ [29]. We evaluated σ_{SI} for $|\cos(\beta-\alpha)| \lesssim 0.01$ and found that σ_{SI} takes the maximum value in the alignment limit. We also found that σ_{SI} can be 0.4 times smaller than that of the alignment limit for the type-II case. Since we are interested in the parameter points where σ_{SI} becomes large, we took the alignment limit throughout our analysis.

JHEP02(2019)028

m_a	m_A	θ	t_β	c_1	c_2
$m_h/2 \sim 100$ GeV	600 GeV	0.1	10	0	$-1 \sim 1$

Table 2. The parameter values and regions discussed in this paper. These values are allowed from the bounds of the Higgs and flavor observables, LHC searches, and electroweak precision measurements for all the THDM-types.

We also assume $c_1 = 0$ and $-1 < c_2 < 1$ in our analysis. In table 2, we summarize the parameter values and regions considered in this paper. As discussed above, these values are consistent with the current bounds from the Higgs and flavor observables, LHC searches, and electroweak precision measurements for all the THDM-types. In section 4, we show the cross section as a function of m_χ by determining g_χ to realize the thermal relic and search the parameter region where the cross section is enhanced.

There are two pseudoscalar mediators, a and A. The interaction terms between the DM and the mediators are

$$\mathcal{L}_{\rm dark} = i\frac{\xi_a^\chi}{2} a\bar{\chi}\gamma^5\chi + i\frac{\xi_A^\chi}{2} A\bar{\chi}\gamma^5\chi, \tag{2.17}$$

where

$$\xi_a^\chi = g_\chi \cos\theta, \quad \xi_A^\chi = g_\chi \sin\theta. \tag{2.18}$$

The scalar trilinear couplings appear from both $V_{\rm THDM}$ and $V_{\rm port}$ as

$$V_{\rm THDM} + V_{\rm port} \supset \sum_{\phi=h,H} \left(-\frac{1}{2} g_{\phi aa}\phi aa - g_{\phi aA}\phi aA - \frac{1}{2} g_{\phi AA}\phi AA \right). \tag{2.19}$$

These couplings induce the DM-nucleon SI scattering at the loop level as we will see in section 3. The expressions of these couplings are shown in appendix A.

There are four types of the Yukawa structures depending on the Z_4 charge assignments of the SM fermions.

$$\mathcal{L}_{\rm Yukawa} \supset \sum_f \left(-\frac{m_f}{v}\right) \left(\xi_h^f h\bar{f}f + \xi_H^f H\bar{f}f + \xi_a^f a\bar{f}i\gamma^5 f + \xi_A^f A\bar{f}i\gamma^5 f \right), \tag{2.20}$$

where f indicates the SM fermion and m_f is its mass. The rescaling factors $\xi_\phi^f (\phi = h, H, a, A)$ under the alignment limit are shown in table 3. As can be seen, the THDM-type dependence appears through the Yukawa couplings of H, a, and A.

3 Direct detection

If DM is a Majorana fermion, the relevant effective operators for the evaluation of the DM-nucleon SI scattering cross section are given by

$$\begin{aligned}\mathcal{L}_{\rm eff} = &\frac{1}{2}\sum_{q=u,d,s} C_q m_q \bar{\chi}\chi\bar{q}q + \frac{1}{2} C_G \left(-\frac{9\alpha_s}{8\pi}\bar{\chi}\chi G^a_{\mu\nu}G^{a\mu\nu} \right) \\ &+ \frac{1}{2}\sum_{q=u,d,s,c,b} \left[C_q^{(1)}\bar{\chi}i\partial^\mu\gamma^\nu\chi\mathcal{O}^q_{\mu\nu} + C_q^{(2)}\bar{\chi}i\partial^\mu i\partial^\nu\chi\mathcal{O}^q_{\mu\nu} \right],\end{aligned} \tag{3.1}$$

JHEP02(2019)028

	ξ_h^u	ξ_h^d	ξ_h^e	ξ_H^u	ξ_H^d	ξ_H^e	ξ_a^u	ξ_a^d	ξ_a^e	ξ_A^u	ξ_A^d	ξ_A^e
Type-I	1	1	1	$-\frac{1}{t_\beta}$	$-\frac{1}{t_\beta}$	$-\frac{1}{t_\beta}$	$\frac{s_\theta}{t_\beta}$	$-\frac{s_\theta}{t_\beta}$	$-\frac{s_\theta}{t_\beta}$	$-\frac{c_\theta}{t_\beta}$	$\frac{c_\theta}{t_\beta}$	$\frac{c_\theta}{t_\beta}$
Type-II	1	1	1	$-\frac{1}{t_\beta}$	t_β	t_β	$\frac{s_\theta}{t_\beta}$	$t_\beta s_\theta$	$t_\beta s_\theta$	$-\frac{c_\theta}{t_\beta}$	$-t_\beta c_\theta$	$-t_\beta c_\theta$
Type-X	1	1	1	$-\frac{1}{t_\beta}$	$-\frac{1}{t_\beta}$	t_β	$\frac{s_\theta}{t_\beta}$	$-\frac{s_\theta}{t_\beta}$	$t_\beta s_\theta$	$-\frac{c_\theta}{t_\beta}$	$\frac{c_\theta}{t_\beta}$	$-t_\beta c_\theta$
Type-Y	1	1	1	$-\frac{1}{t_\beta}$	t_β	$-\frac{1}{t_\beta}$	$\frac{s_\theta}{t_\beta}$	$t_\beta s_\theta$	$-\frac{s_\theta}{t_\beta}$	$-\frac{c_\theta}{t_\beta}$	$-t_\beta c_\theta$	$\frac{c_\theta}{t_\beta}$

Table 3. The rescaling factors of the Yukawa couplings under the alignment limit, where $s_\theta = \sin\theta$ and $c_\theta = \cos\theta$.

For proton	
$f_{T_u}^p$	0.0153
$f_{T_d}^p$	0.0191
$f_{T_s}^p$	0.0447

For neutron	
$f_{T_u}^n$	0.0110
$f_{T_d}^n$	0.0273
$f_{T_s}^n$	0.0447

Table 4. Numerical values of matrix elements which are taken from the default value of `micrOMEGAs` [36]. The left panel shows the value for the proton, and the right for the neutron.

where $\mathcal{O}_{\mu\nu}^q$ is the twist-2 operator for quark q,

$$\mathcal{O}_{\mu\nu}^q = \frac{i}{2}\bar{q}\left(D_\mu\gamma_\nu + D_\nu\gamma_\mu - \frac{1}{2}g_{\mu\nu}\not{D}\right)q. \tag{3.2}$$

We use the following relations to evaluate the SI cross section from these operators [35],

$$\langle N \,|\, m_q\bar{q}q \,|\, N\rangle = m_N f_{T_q}^N, \tag{3.3}$$

$$-\frac{9\alpha_s}{8\pi}\left\langle N \,\middle|\, G_{\mu\nu}^a G^{a\mu\nu} \,\middle|\, N\right\rangle = m_N f_{T_G}^N, \tag{3.4}$$

$$\left\langle N \,\middle|\, \mathcal{O}_{\mu\nu}^q \,\middle|\, N\right\rangle = \frac{1}{m_N}\left(p_\mu p_\nu - \frac{1}{4}m_N^2 g_{\mu\nu}\right)\Big(q^N(2) + \bar{q}^N(2)\Big), \tag{3.5}$$

where N stands for a nucleon (p, n), and m_N is its mass. The numerical values of the matrix elements ($f_{T_q}^N$) and the second moments of the parton distribution functions (PDFs) for the quark and anti-quark ($q^N(2)$ and $\bar{q}^N(2)$) are given in tables 4 and 5, respectively. The gluon matrix element ($f_{T_G}^N$) is given as follows: [23]

$$f_{T_G}^N = 1 - \sum_{q=u,d,s} f_{T_q}^N. \tag{3.6}$$

The values of $q^N(2)$ and $\bar{q}^N(2)$ are calculated at the scale $\mu = m_Z$, where m_Z is Z boson mass. The DM-nucleon SI scattering cross section is given by

$$\sigma_{\rm SI} = \frac{1}{\pi}\left(\frac{m_\chi m_N}{m_\chi + m_N}\right)^2 |C_N|^2, \tag{3.7}$$

JHEP02(2019)028

Second moment at $\mu = m_Z$			
$u^p(2)$	0.22	$\overline{u}^p(2)$	0.034
$d^p(2)$	0.11	$\overline{d}^p(2)$	0.036
$s^p(2)$	0.026	$\overline{s}^p(2)$	0.026
$c^p(2)$	0.019	$\overline{c}^p(2)$	0.019
$b^p(2)$	0.012	$\overline{b}^p(2)$	0.012

Table 5. Numerical values of the second moments for quark distribution functions for proton. These values are evaluated at the scale $\mu = m_Z$ by using the CTEQ PDFs [37]. The values for neutron are given by exchanging up and down quarks in the table.

where

$$C_N = m_N \left[\sum_{q=u,d,s} C_q f_{T_q}^N + C_G f_{T_G}^N + \frac{3}{4} \sum_{q=u,d,s,c,b} \left(m_\chi C_q^{(1)} + m_\chi^2 C_q^{(2)} \right) \left(q^N(2) + \overline{q}^N(2) \right) \right]. \tag{3.8}$$

The Wilson coefficients (C_q, C_G, $C_q^{(1)}$, and $C_q^{(2)}$) are model dependent parts. In the rest of this section, we calculate these Wilson coefficients at the leading order.

In the pseudoscalar mediator DM model, all of the Wilson coefficients in eq. (3.1) are zero at the tree-level. Diagrams at the one-loop level give the leading order contributions to C_q, $C_q^{(1)}$, and $C_q^{(2)}$. For C_G, the leading order contribution arises at the two-loop level. Note that the gluon matrix element is defined with the one-loop factor in eq. (3.4), and thus the contribution from C_G to $\sigma_{\rm SI}$ is the same order of magnitude as the contributions from the other Wilson coefficients. For the later convenience, we divide C_q and C_G into the contributions from triangle and box diagrams. We introduce the following notations.

$$C_q = C_q^{\rm tri} + C_q^{\rm box}, \tag{3.9}$$

$$C_G = C_G^{\rm tri} + C_G^{\rm box}, \tag{3.10}$$

$$C_q^{(1)} = C_q^{(1)\rm box}, \tag{3.11}$$

$$C_q^{(2)} = C_q^{(2)\rm box}. \tag{3.12}$$

3.1 Triangle diagrams

In the following, we show the effective operators from the triangle diagrams shown in figure 1.

First, we consider the triangle diagrams with the light quark ($q = u, d, s$) in the external line. Each diagram generates the following effective interaction between DM and quark q,

$$\mathcal{L}_{\rm eff} \supset \frac{1}{2} \sum_{q=u,d,s} C_q^{\rm tri} m_q \bar{\chi}\chi\bar{q}q, \tag{3.13}$$

where

$$C_q^{\rm tri} = -\sum_{\phi=h,H} \frac{\xi_\phi^q}{m_\phi^2 v} C_{\phi\chi\chi}. \tag{3.14}$$

JHEP02(2019)028

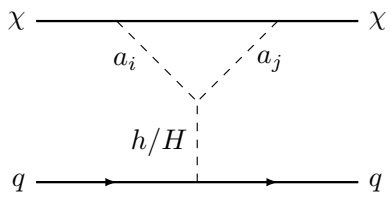

Figure 1. Triangle diagrams which contribute to the DM-nucleon SI scattering. a_i indicates the pseudoscalar mediators, a and A. q in the external line stands for quarks. The diagrams with each of the light quarks (u, d, s) contribute to $\bar{\chi}\chi\bar{q}q$. The diagrams with heavy quarks (c, b, t) contribute to $\bar{\chi}\chi G^a_{\mu\nu}G^{a\mu\nu}$.

The expression of the effective $\phi\bar{\chi}\chi$ coupling coefficient ($\phi = h, H$), $C_{\phi\chi\chi}$, is as follows:

$$C_{\phi\chi\chi} = \frac{-m_\chi}{(4\pi)^2}\Bigg\{ g_{\phi aa}(\xi^\chi_a)^2 \left[\frac{\partial}{\partial p^2}B_0(p^2, m_a^2, m_\chi^2)\right]_{p^2=m_\chi^2} + g_{\phi AA}(\xi^\chi_A)^2 \left[\frac{\partial}{\partial p^2}B_0(p^2, m_A^2, m_\chi^2)\right]_{p^2=m_\chi^2} + \frac{2g_{\phi aA}\xi^\chi_A\xi^\chi_a}{m_A^2 - m_a^2}\left[B_1(m_\chi^2, m_A^2, m_\chi^2) - B_1(m_\chi^2, m_a^2, m_\chi^2)\right]\Bigg\}. \tag{3.15}$$

The definitions of the loop functions B_0 and B_1 are given in appendix C.1.

Next, we calculate the triangle diagrams which contribute to the effective DM-gluon coupling, C_G. There is the relation between $\bar{\chi}\chi G^a_{\mu\nu}G^{a\mu\nu}$ and $\bar{\chi}\chi\bar{Q}Q$ via [23]

$$m_Q\bar{Q}Q = -\frac{\alpha_s}{12\pi}G^a_{\mu\nu}G^{a\mu\nu}, \tag{3.16}$$

where Q indicates the heavy quark (c, b, t). Using this relation, $C_G^{\rm tri}$ can be expressed with $C_Q^{\rm tri}$ as follows:

$$C_G^{\rm tri} = \sum_{Q=c,b,t}\frac{2}{27}C_Q^{\rm tri}, \tag{3.17}$$

where $C_Q^{\rm tri}$ is obtained by substituting q to Q in eq. (3.14).

3.2 Box diagrams

In the following, we show the effective operators from the box diagrams.

3.2.1 DM-quark scalar operators from box diagrams

We derive the contributions to C_q, $C_q^{(1)}$, and $C_q^{(2)}$ in eq. (3.1) from the box diagrams shown in figure 2. Because the quark in the external line is non-relativistic, we expand the amplitude by the external quark momentum and derive the effective operators. After that, we decompose these effective operators into the scalar and twist-2 operators as follows:

$$\mathcal{L}_{\rm eff} \supset \frac{1}{2}C_q^{\rm box}m_q\bar{\chi}\chi\bar{q}q + \frac{1}{2}\left[C_q^{(1)\rm box}\bar{\chi}i\partial^\mu\gamma^\nu\chi\mathcal{O}^q_{\mu\nu} + C_q^{(2)\rm box}\bar{\chi}i\partial^\mu i\partial^\nu\chi\mathcal{O}^q_{\mu\nu}\right]. \tag{3.18}$$

JHEP02(2019)028

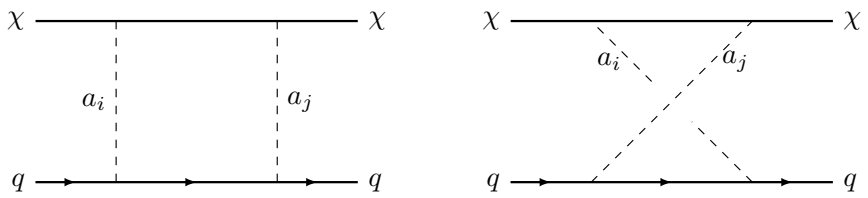

Figure 2. The box diagrams which induce the DM-quark effective operators, where $a_i = a, A$.

The Wilson coefficients are

$$C_q^{\rm box} = \frac{-m_\chi}{(4\pi)^2}\left(\frac{m_q}{v}\right)^2 \left\{ \frac{(\xi_a^\chi \xi_a^q)^2}{m_a^2}\left[G(m_\chi^2,0,m_a^2) - G(m_\chi^2,m_a^2,0)\right] \right.$$
$$+\frac{(\xi_A^\chi \xi_A^q)^2}{m_A^2}\left[G(m_\chi^2,0,m_A^2) - G(m_\chi^2,m_A^2,0)\right]$$
$$\left. +2\frac{\xi_A^\chi \xi_a^\chi \xi_A^q \xi_a^q}{m_A^2 - m_a^2}\left[G(m_\chi^2,m_A^2,0) - G(m_\chi^2,m_a^2,0)\right] \right\}, \tag{3.19}$$

$$C_q^{(1){\rm box}} = \frac{-8}{(4\pi)^2}\left(\frac{m_q}{v}\right)^2 \left\{ \frac{(\xi_a^\chi \xi_a^q)^2}{m_a^2}\left[X_{001}(p^2,m_\chi^2,0,m_a^2) - X_{001}(p^2,m_\chi^2,m_a^2,0)\right] \right.$$
$$+\frac{(\xi_A^\chi \xi_A^q)^2}{m_A^2}\left[X_{001}(p^2,m_\chi^2,0,m_A^2) - X_{001}(p^2,m_\chi^2,m_A^2,0)\right]$$
$$\left. +2\frac{\xi_A^\chi \xi_a^\chi \xi_A^q \xi_a^q}{m_A^2 - m_a^2}\left[X_{001}(p^2,m_\chi^2,m_A^2,0) - X_{001}(p^2,m_\chi^2,m_a^2,0)\right] \right\}, \tag{3.20}$$

$$C_q^{(2){\rm box}} = \frac{-4m_\chi}{(4\pi)^2}\left(\frac{m_q}{v}\right)^2 \left\{ \frac{(\xi_a^\chi \xi_a^q)^2}{m_a^2}\left[X_{111}(p^2,m_\chi^2,0,m_a^2) - X_{111}(p^2,m_\chi^2,m_a^2,0)\right] \right.$$
$$+\frac{(\xi_A^\chi \xi_A^q)^2}{m_A^2}\left[X_{111}(p^2,m_\chi^2,0,m_A^2) - X_{111}(p^2,m_\chi^2,m_A^2,0)\right]$$
$$\left. +2\frac{\xi_A^\chi \xi_a^\chi \xi_A^q \xi_a^q}{m_A^2 - m_a^2}\left[X_{111}(p^2,m_\chi^2,m_A^2,0) - X_{111}(p^2,m_\chi^2,m_a^2,0)\right] \right\}, \tag{3.21}$$

where

$$G(m_\chi^2, m_1^2, m_2^2) = 6X_{001}(m_\chi^2, m_\chi^2, m_1^2, m_2^2) + m_\chi^2 X_{111}(m_\chi^2, m_\chi^2, m_1^2, m_2^2). \tag{3.22}$$

The definitions of the loop functions X_{001} and X_{111} are given in appendix C.2. The details of the derivation of the coefficients in eqs. (3.19)–(3.21) are given in appendix B.1.

3.2.2 DM-gluon scalar operator from box diagrams

We calculate the contribution from the box diagrams to C_G. For the box diagrams, the procedure of the triangle diagrams cannot be applied due to the following reasons: first, for $m_Q > m_\chi, m_a, m_A$, we cannot obtain the effective operators with the heavy quark $\bar{\chi}\chi\bar{Q}Q$ by expanding the amplitude by the quark momentum as done in section 3.2.1. In particular,

JHEP02(2019)028

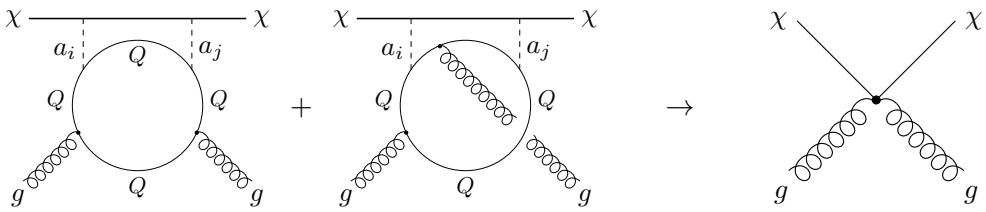

Figure 3. The two-loop diagrams for the DM-gluon effective operator, where $Q = c, b, t$.

the loop calculation is mandatory for $m_t > m_a$ as we will see in later. Second, even if $m_Q \ll m_\chi, m_a, m_A$, the second diagrams in figure 3 are not included if we derive $C_G^{\rm box}$ from $C_Q^{\rm box}$ by using eq. (3.16). Thus, it is necessary to calculate the two-loop diagrams shown in figure 3 and to read out the effective operator $\bar{\chi}\chi G^a_{\mu\nu}G^{a\mu\nu}$ directly. We use the Fock-Schwinger gauge for the gluon field [38]. This gauge enables us to calculate the effective operator much more transparently [39]. In the end, we find the following effective operator from these two-loop diagrams [40].

$$\mathcal{L}_{\rm eff} \supset \frac{1}{2} C_G^{\rm box} \left(\frac{-9\alpha_s}{8\pi} \overline{\chi}\chi G^a_{\mu\nu} G^{a\mu\nu} \right). \tag{3.23}$$

The Wilson coefficient is given by

$$C_G^{\rm box} = \sum_{Q=c,b,t} \frac{-m_\chi}{432\pi^2} \left(\frac{m_Q}{v}\right)^2 \left[(\xi_a^\chi \xi_a^Q)^2 \frac{\partial F(m_a^2)}{\partial m_a^2} + (\xi_A^\chi \xi_A^Q)^2 \frac{\partial F(m_A^2)}{\partial m_A^2} + 2\xi_A^\chi \xi_a^\chi \xi_A^Q \xi_a^Q \frac{\left[F(m_A^2) - F(m_a^2)\right]}{m_A^2 - m_a^2} \right], \tag{3.24}$$

where

$$\begin{aligned} F(m_a^2) = \int_0^1 dx \Big\{ & 3Y_1(p^2, m_\chi^2, m_a^2, m_Q^2) \\ & - m_Q^2 \frac{(2 + 5x - 5x^2)}{x^2(1-x)^2} Y_2(p^2, m_\chi^2, m_a^2, m_Q^2) \\ & - 2m_Q^4 \frac{(1 - 2x + 2x^2)}{x^3(1-x)^3} Y_3(p^2, m_\chi^2, m_a^2, m_Q^2) \Big\}. \end{aligned} \tag{3.25}$$

The definitions of the loop functions Y_1, Y_2, and Y_3 are shown in appendix C.3. The expression for $\partial F(m_a^2)/\partial m_a^2$ is shown in appendix C.5. The details of the derivation of $C_G^{\rm box}$ are given in appendix B.2.

4 Numerical analysis

In this section, we show our numerical analysis for the DM-nucleon SI scattering cross section ($\sigma_{\rm SI}$). We focus on the region of the parameter space where the DM thermal relic abundance matches the measured value of the DM energy density, $\Omega h^2 = 0.1198 \pm 0.0015$ [41]. In section 4.1, we show that it is easy to realize the correct DM energy density by choosing g_χ appropriately. Using the value of g_χ, we calculate $\sigma_{\rm SI}$. In section 4.2, we

JHEP02(2019)028

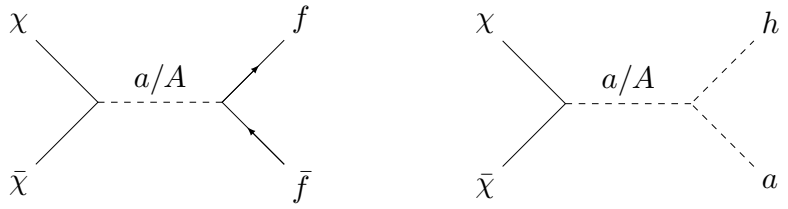

Figure 4. The dominant annihilation diagrams at the tree-level, where f indicates the SM fermion.

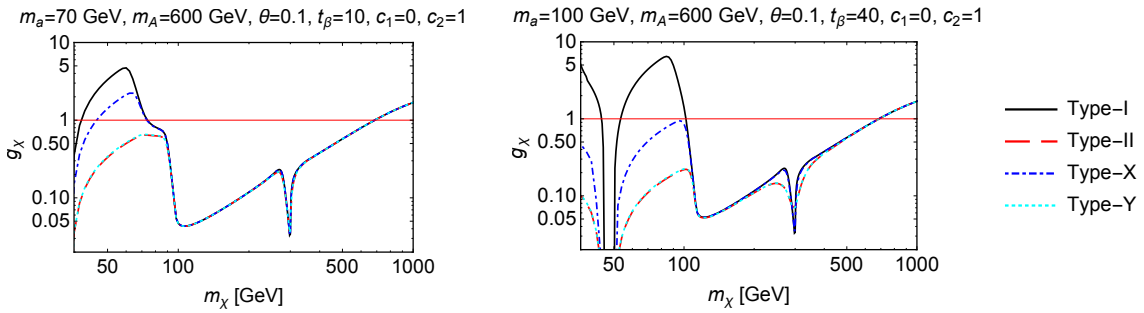

Figure 5. The DM-pseudoscalar coupling g_χ as a function of m_χ. The left panel shows g_χ for $m_a = 70\,\text{GeV}$ and $t_\beta = 10$, and the right for $m_a = 100\,\text{GeV}$ and $t_\beta = 40$. The other parameters are $m_A = 600\,\text{GeV}$, $\theta = 0.1$, $c_1 = 0$, $c_2 = 1$ for both of the panels. The black solid, red dashed, blue dot-dashed, and cyan dotted lines show the type-I, II, X, and Y, respectively. The red horizontal line indicates $g_\chi = 1$. The coupling of the type-Y turns out to be almost the same result as that of the type-II.

show the comparison of our result with the previous one [11]. We find that the gluon contribution through the box diagrams was drastically changed from the results in [11]. In section 4.3, we discuss the effect of the scalar quartic coupling which enhances σ_{SI}. We find that some parameter points are within the reach of the XENONnT [20] and LZ experiments [21].

4.1 Determination of g_χ through the DM thermal relic abundance

We discuss the DM pair annihilation and determine g_χ to realize the measured value of the DM energy density by the thermal relic abundance. The dominant annihilation processes are shown in figure 4. Note that the $f\bar{f}$ channel, where f is the SM fermion, depends on the THDM-types through the rescaling factors of the Yukawa couplings, ξ_a^f and ξ_A^f. On the other hand, the scalar channel is independent of the THDM-type.

Figure 5 shows g_χ as a function of m_χ for the four THDM-types. Here we use `micrOMEGAs` [36] to calculate the DM thermal relic abundance for the determination of g_χ. We find that g_χ becomes suddenly small around the funnel position where $m_\chi \sim m_{a_i}/2$ $(a_i = a, A)$. In these regions, the s-channel amplitude becomes very large because it is proportional to $(s - m_{a_i}^2 + i m_{a_i}\Gamma_{a_i})^{-1}$, where s is the invariant mass square and Γ_{a_i} is the decay width of a_i. As a result, g_χ has to be small to obtain $\Omega h^2 \sim 0.12$, otherwise the relic abundance becomes too small. The coupling also becomes small after the new annihilation channel $\chi\bar{\chi} \to ha$ opens. As can be seen in figure 5, g_χ suddenly begins to decrease at

JHEP02(2019)028

	$m_\chi \sim 50\,\mathrm{GeV}$	$m_\chi \sim 300\,\mathrm{GeV}$
Type-I	$b\bar{b}$	ha
Type-II	$b\bar{b}$	$b\bar{b}$
Type-X	$\tau^-\tau^+$	$\tau^-\tau^+$
Type-Y	$b\bar{b}$	$b\bar{b}$

Table 6. The dominant annihilation channels of each THDM-type near the funnel positions. The parameters are $m_a = 100\,\mathrm{GeV}$, $m_A = 600\,\mathrm{GeV}$, $\theta = 0.1$, $t_\beta = 40$, $c_1 = 0$, $c_2 = 1$.

$m_\chi \sim (m_h + m_a)/2$. For the larger m_χ, the annihilation amplitude is suppressed by m_χ^{-2}, and g_χ increases in proportion to m_χ^2. We find that $g_\chi > 1$ for $m_\chi \geq 690\,\mathrm{GeV}$.

Figure 5 also shows the THDM-type dependence of g_χ. The type dependence appears in the region where the annihilation channel $\chi\bar{\chi} \to f\bar{f}$ is dominant. For $m_\chi \leq (m_h + m_a)/2$, the channel $\chi\bar{\chi} \to ha$ is kinematically forbidden, and thus the type dependence appears in g_χ. For the type-I, all of the Yukawa couplings are suppressed by large t_β, and g_χ tends to be large to keep $\Omega h^2 \sim 0.12$. For the type-II and the type-Y, g_χ is almost the same. This is because the difference in the charged lepton sector is negligible if the down-type quark Yukawa couplings have t_β enhancement. The annihilation channel $\chi\bar{\chi} \to ha$ dominates the process once allowed kinematically, and thus g_χ becomes type independent for $m_\chi > (m_h + m_a)/2$. Around $m_\chi \sim m_A/2$, however, we find the type dependence of g_χ again. This is because the annihilation channel to $f\bar{f}$ through the mediator A again dominates the annihilation process by t_β enhancement. In table 6, we show the dominant annihilation channels near the funnel positions for each of the THDM-types.

4.2 Comparison with the previous results

In the following, we compare our result with the previous one in [11] at the benchmark point with $m_a = 100\,\mathrm{GeV}$, $m_A = 600\,\mathrm{GeV}$, $\theta = 0.1$, $t_\beta = 40$, $g_\chi = 1$, and the Yukawa structure is the type-II.[7] We also choose $c_1 = c_2 = 0$ for the comparison. If the heavy scalar masses are degenerated and $c_1 = c_2 = 0$ under the alignment limit, then $g_{Ha_ia_j} = 0$ where $a_i = a, A$ (see, appendix A). We use `LoopTools` [42] in the numerical calculations of the loop functions. Unless otherwise noted, the previous work means [11] in this section 4.2.

There are two improvements in our analysis of the triangle diagrams. First, we read out the scalar trilinear couplings not only from V_{port} but also from V_{THDM}. We find that the values of g_{haa} and g_{haA} do not change drastically at the benchmark point. On the other hand, the value of g_{hAA} changes largely. However, the diagram with g_{hAA} gives the smaller contribution than the diagrams with g_{haa} and g_{haA}. As a result, the numerical impact of this improvement is negligible. Second, we include all of the triangle diagrams into our analysis. The diagrams with g_{haA} and g_{hAA} were not included in the previous work. However, these diagrams are also important as pointed out in [13]. In figure 6, we show the contributions from each of the triangle diagrams to C_G^{tri}. The red dashed, blue dot-dashed, and green dotted lines are the contributions from the haa-diagram, the haA-diagram, and

[7] Note that this combination of the value of t_β and m_A with the type-II THDM is already excluded by LHC experiments [33]. We take this point only for the comparison.

JHEP02(2019)028

the hAA-diagram, respectively. The black solid line shows the total contribution from these three triangle diagrams. As can be seen from the figure, the effect from the haa-diagram is dominant. We also find that the effect from the haA-diagram cannot be negligible because $|g_{haa}| < |g_{haA}|$ at the benchmark point. Moreover, the relative sign between the haa-diagram and the haA-diagram is opposite, and they partially cancel each other. At $m_\chi = 1\,\text{TeV}$, for example, we find that the total coefficient turns out to be 0.6 times that of the haa-diagram. Therefore, the contribution from the triangle diagrams is overestimated in the previous work.

As for the box diagrams, there are also two improvements. First, as we mentioned in section 3.2.1, we perform the irreducible decomposition into the scalar and twist-2 operators. After this decomposition, we find new contributions to C_q^{box} which were not included in the previous work. See, appendix B.1 for the details. We show the numerical impact of the irreducible decomposition in the first two panels in figure 7. The black solid line in the upper (central) panel shows C_G^{box} derived from C_c^{box} (C_b^{box}) without irreducible decomposition by using the relation in eq. (3.16), which was done in the previous work. The blue dotted lines are the same but with the irreducible decomposition. We find that the difference between the black and blue lines is small numerically. Second, we evaluate C_G^{box} by calculating the two-loop diagrams shown in figure 3. The red dashed lines in figure 7 show the contributions to C_G^{box} which are derived by the two-loop calculations. As for the contributions from the charm and bottom quarks, we find that C_G^{box} read out by using eq. (3.16) is 40% of the full two-loop calculations. Therefore, the previous work underestimated the contributions from the box diagrams with the charm and bottom quarks to C_G. The contribution from the top quark is shown in the last panel in figure 7. The black solid line shows C_G^{box} derived from C_t^{box} without irreducible decomposition by using the relation in eq. (3.16), which was done in the previous work. We use eq. (A.3) in [11] to evaluate C_t^{box}.[8] The last panel clearly shows that the contribution from the top quark was overestimated in the previous work. Thus, it is not justified to relate C_G^{box} with C_Q^{box} using eq. (3.16).

As can be seen from figure 7, the scattering diagrams with the bottom loop give the dominant contribution to C_G^{box}, and thus C_G^{box} was underestimated in the previous work. Comparing figures 6 and 7, we find that the contribution from the box diagrams is smaller than that from the triangle diagrams in spite of taking the large t_β and the type-II THDM.

4.3 The DM-nucleon scattering cross section

We discuss the DM-nucleon scattering cross section numerically. In the following, we focus on the triangle diagrams with h and search the parameter region where the amplitude of these diagrams becomes large. Note that these diagrams are independent of the THDM-types under the alignment limit, and thus the cross section is type independent quantitatively. As shown in figure 1, there are also the triangle diagrams with H instead of h, but the amplitude of these diagrams is suppressed by $(m_h/m_H)^2$.

[8] We have found that the overall sign of C_Q^{box} shown in section 3.2.1 disagrees with the previous work. In figure 7, we show the comparison with the absolute value of the coefficient.

JHEP02(2019)028

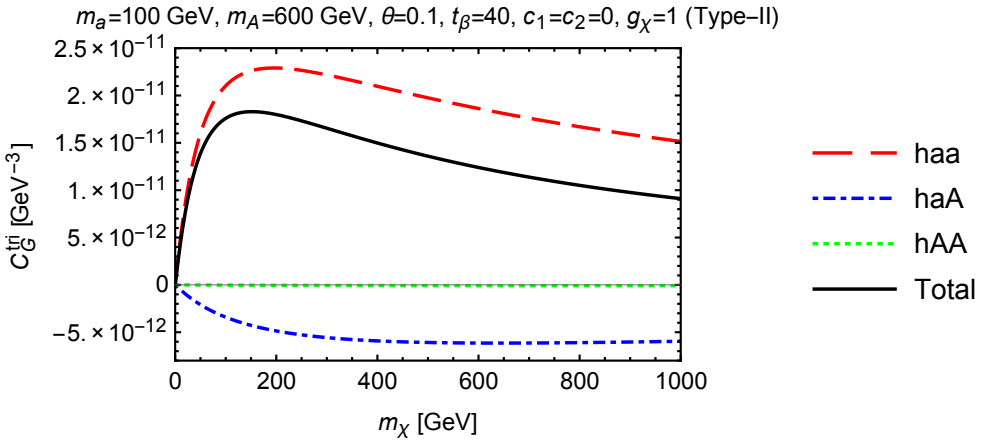

Figure 6. The contributions from each of the triangle diagrams to $C_G^{\rm tri}$. The parameters are $m_a = 100\,\text{GeV}$, $m_A = 600\,\text{GeV}$, $\theta = 0.1$, $t_\beta = 40$, $c_1 = c_2 = 0$, and $g_\chi = 1$. The THDM-type is the type-II. The red dashed, blue dot-dashed, and green dotted lines show the contributions from the haa-diagram, the haA-diagram, and the hAA-diagram, respectively. The black solid line shows the total of these contributions.

A possible way to enhance $\sigma_{\rm SI}$ is to make g_{haa} large. As can be seen from the expression of g_{haa} in eq. (A.8), the contributions from c_1 and c_2 terms to g_{haa} are essential for small θ. In particular, the c_2 term gives a crucial contribution to g_{haa} for the large t_β regime. Another possibility to enhance $\sigma_{\rm SI}$ is to make m_a as light as possible. If m_a is light, the suppression from the loop functions of the triangle diagrams with a is weakened. However, we cannot make m_a arbitrary small. We find that $m_a \geq m_h/2$. The constraint on m_a comes from the bound on the branching ratio of the SM Higgs boson. In the region $m_a \leq m_h/2$, this model has a new decay channel of the Higgs boson, $h \to 2a$. The decay width is given by [6]

$$\Gamma_{h\to 2a} = \frac{g_{haa}^2}{32\pi m_h}\sqrt{1-\frac{4m_a^2}{m_h^2}}. \tag{4.1}$$

This decay width is proportional to g_{haa}^2. Note that we are considering the large g_{haa} region to enhance $\sigma_{\rm SI}$. Consequently, this decay width becomes large and gives a strong constraint on m_a. For example, we find that $\Gamma_{h\to 2a} = 4.59\,\text{GeV}$ at the point $m_a = 60\,\text{GeV}$, $m_A = 600\,\text{GeV}$, $\theta = 0.1$, $t_\beta = 10$, $c_1 = 0$, and $c_2 = 1$. This value is much larger than the SM Higgs width. The current bound on the Higgs branching ratio into BSM particles is given by the ATLAS experiment [29],

$$\text{BR(BSM)} < 0.26. \tag{4.2}$$

The result from the CMS experiment also disfavors the large branching ratio of the Higgs boson into new particles [34]. We conclude that the parameter region $m_a \leq m_h/2$ is excluded.

In figure 8, we show the predicted cross section in this model. We take $m_a = 100\,\text{GeV}$, $m_A = 600\,\text{GeV}$, $\theta = 0.1$, $t_\beta = 10$, $c_1 = 0$, and $c_2 = 1$ and show the plot in 10 GeV <

JHEP02(2019)028

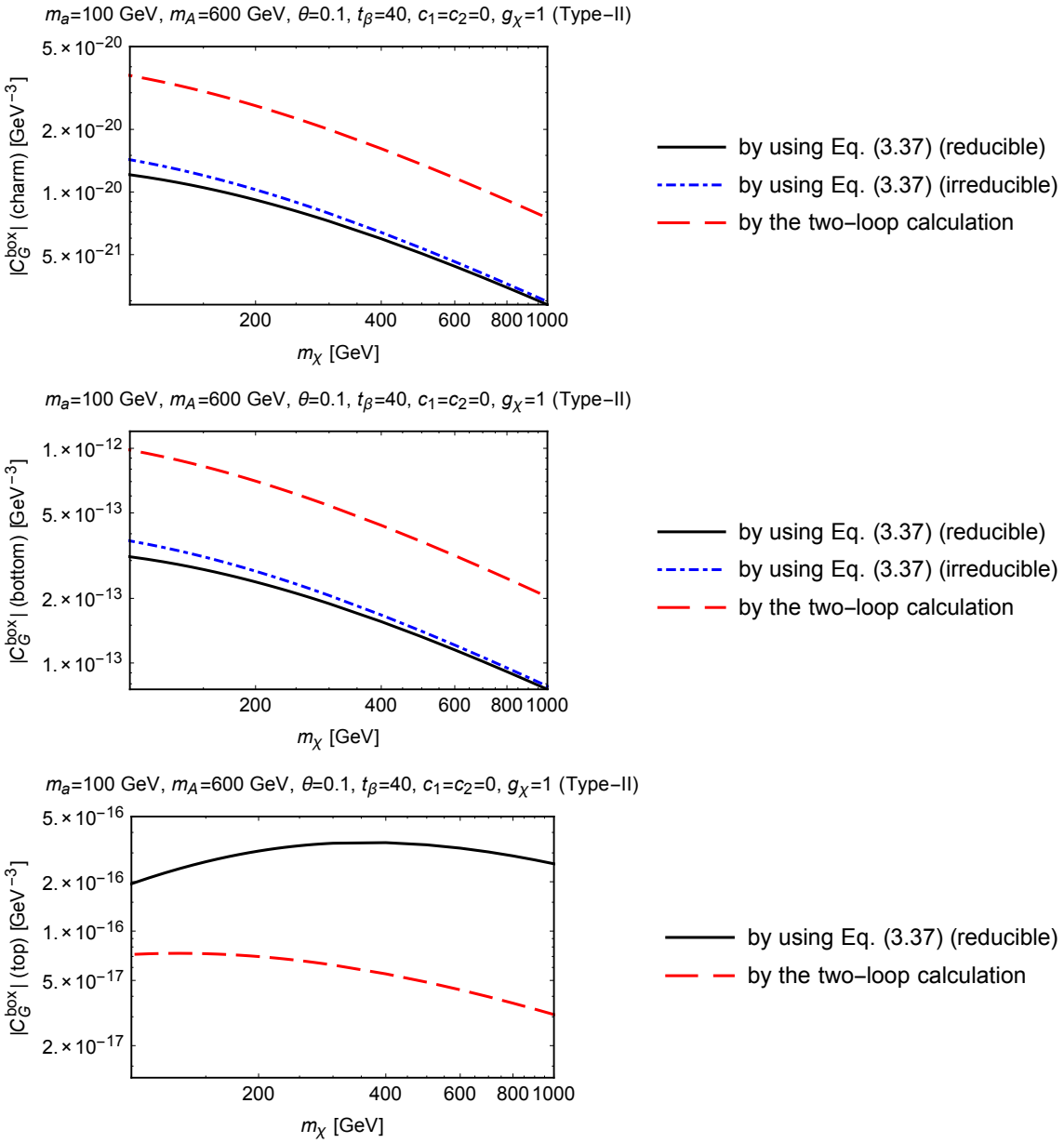

Figure 7. The contributions from each of the box diagrams to $C_G^{\rm box}$. The parameters are $m_a = 100\,\text{GeV}$, $m_A = 600\,\text{GeV}$, $\theta = 0.1$, $t_\beta = 40$, $c_1 = c_2 = 0$, and $g_\chi = 1$. The THDM-type is the type-II. The upper, central, and bottom panels show the contributions from the charm, bottom, and top quarks, respectively. The black solid lines show the contributions which are derived from $C_Q^{\rm box}$ $(Q = c, b, t)$ without irreducible decomposition by using the relation in eq. (3.16). The blue dotted lines are the same but with the irreducible decomposition. The red dashed lines show the contributions which are derived from the two-loop calculations.

JHEP02(2019)028

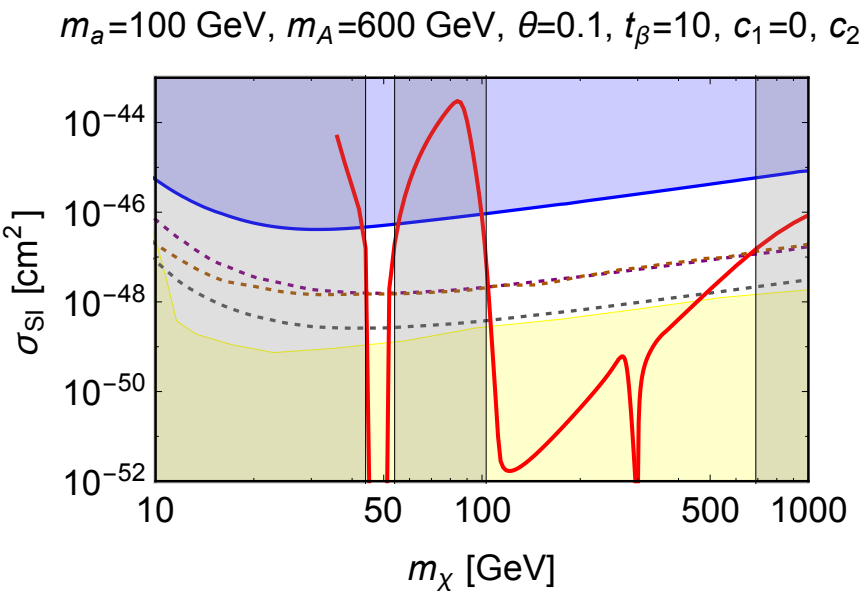

Figure 8. The red solid line shows the predicted SI cross section of this model with $m_a = 100\,\text{GeV}$, $m_A = 600\,\text{GeV}$, $\theta = 0.1$, $t_\beta = 10$, $c_1 = 0$, and $c_2 = 1$. The regions where $g_\chi > 1$ are shown as the gray region. The blue region is excluded by the latest result of the XENON1T experiment [3]. The purple, brown, and gray dotted lines indicate the future sensitivities of the XENONnT [20], LZ [21], and DARWIN experiments [22], respectively. The yellow region is below the neutrino floor [19].

$m_\chi < 1$ TeV. In the discontinuous part of the plot, we cannot find the solution of g_χ which realizes $\Omega h^2 \sim 0.12$. The region where $g_\chi > 1$ is shown as the gray region. The current bound, future prospects, and neutrino floor of the direct detection experiments are also shown in the figure. The blue regions are already excluded by the latest result of the XENON1T experiment [3]. The purple, brown, and gray dotted lines indicate the future sensitivities of the XENONnT [20], LZ [21], and DARWIN experiments [22], respectively. The yellow regions are below the neutrino floor [19].

As can be seen, we find that $g_\chi > 1$ and the cross section is larger than the upper bound from the XENON1T experiment [3] in almost all of the region where $m_\chi < (m_h + m_a)/2$ except for the funnel position of the light pseudoscalar, $m_\chi \sim m_a/2$. In addition, the previous work [11] has pointed out that the light DM mass region is excluded by the indirect detection experiments. From above reasons, we focus on the heavier DM mass region, $100\,\text{GeV} < m_\chi < 1\,\text{TeV}$, and search the parameter space where the cross section becomes large.

In figure 9, we show the four benchmark points which have the different combinations of c_2 and m_a. Here, we fix the parameters at $m_A = 600\,\text{GeV}$, $\theta = 0.1$, $t_\beta = 10$, and $c_1 = 0$. These benchmark points are all allowed from the current constraints as we mentioned in section 2.

We show the case for $|c_2| = 0.5$ in the upper panels, and for $|c_2| = 1$ in the lower panels. In each panel, the red line shows the positive c_2, the blue line shows the negative c_2, and the black line shows $c_2 = 0$. We show the case for $m_a = 70\,\text{GeV}$ in the left panels,

JHEP02(2019)028

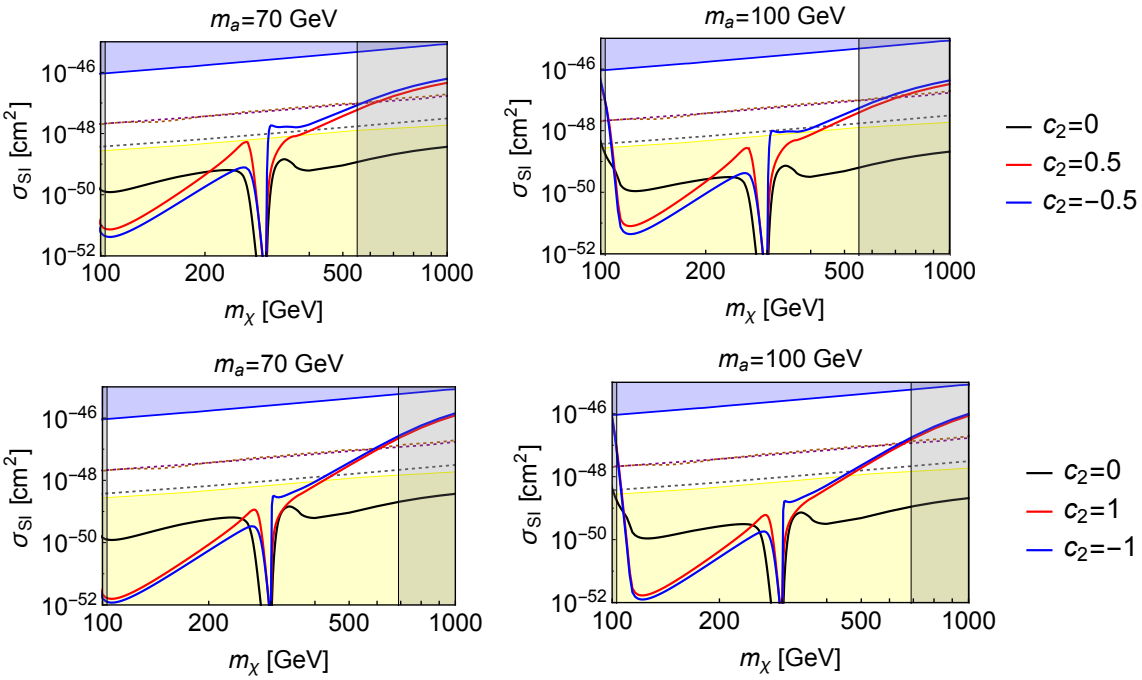

Figure 9. The SI cross section at the four benchmark points. The upper panels show the case for $|c_2| = 0.5$, and the lower for $|c_2| = 1$. The left panels show the case for $m_a = 70\,\text{GeV}$, and the right for $m_a = 100\,\text{GeV}$. The other parameters are $m_A = 600\,\text{GeV}$, $\theta = 0.1$, $t_\beta = 10$, $c_1 = 0$ for all the panels. The regions where $g_\chi > 1$ are shown as the gray region. The blue regions are excluded by the latest result of the XENON1T experiment [3]. The purple, brown, and gray dotted lines indicate the future sensitivities of the XENONnT [20], LZ [21], and DARWIN experiments [22], respectively. The yellow regions are below the neutrino floor [19].

and $m_a = 100\,\text{GeV}$ in the right panels. The DM coupling g_χ becomes larger than 1 in the gray region. The current bound, future prospects, and background of the direct detection experiments shown in figure 9 are the same as those shown in figure 8.

From the figure, we find that σ_{SI} strongly depends on c_2. In particular, σ_{SI} becomes large for $m_\chi \gtrsim 400\,\text{GeV}$ if c_2 is nonzero. This is because g_{haa} becomes large by the effect of c_2 as we mentioned above. We also find that σ_{SI} for $m_a = 70\,\text{GeV}$ is larger than that for $m_a = 100\,\text{GeV}$ as is expected. At these benchmark points, we find the large region where σ_{SI} is above the neutrino floor while keeping $g_\chi \leq 1$. For $c_2 = 1$, $m_a = 70\,\text{GeV}$, and $600\,\text{GeV} \leq m_\chi \leq 690\,\text{GeV}$, σ_{SI} is above the future prospect lines of the XENONnT [20] and LZ experiments [21] with $g_\chi \leq 1$.

We also have checked the cross section of the different types of the THDM and found that σ_{SI} in the large m_χ region is type independent.

5 Conclusions

In this paper, we have discussed the physics of the DM direct detection in the pseudoscalar mediator DM model. The tree-level amplitude of the DM-nucleon elastic scattering in

JHEP02(2019)028

this model is negligible because it is proportional to the momentum transfer in the non-relativistic limit. At the loop level, however, there are the diagrams which induce the DM-nucleon SI scattering. Thus, it is necessary to calculate the loop corrections to compare the model prediction with the direct detection experiments.

We have revisited the loop corrections to the cross section calculated in [11] and improved their analysis with the following points. For the triangle diagrams, we read out the scalar trilinear couplings not only from $V_{\rm port}$ but also from $V_{\rm THDM}$ as shown in eq. (2.19). We also included the diagrams with the heavy mediator A into our analysis as pointed out in [13]. As a result, we found that the scattering amplitude of the triangle diagrams was overestimated in [11]. This is because the cancellation between the haa-diagram and the haA-diagram is not negligible numerically. For the box diagrams, we decomposed the effective operators into the scalar and twist-2 operators. This decomposition gives the new contributions to the scalar operator, but we found that their effects are not significant. In addition, we read out the DM-gluon scalar operator by calculating all the relevant two-loop diagrams. We found that the contributions from the charm and bottom quarks to $C_G^{\rm box}$ were underestimated in [11]. On the other hand, the contribution from the top quark was overestimated. These results clearly show that it is no longer justified to relate $C_G^{\rm box}$ with $C_Q^{\rm box}$ using eq. (3.16).

In section 4.3, we searched the region where the DM-nucleon scattering cross section becomes large. We found the two interesting cases. First, if c_2 is nonzero, the cross section is enhanced in the large m_χ region. This is because the contribution from c_2 to g_{haa} appears without the suppression of the mixing angle and t_β. The interaction term proportional to c_2 is not included in the previous works, [6], [11] and [13]. Thus, our analysis has revealed the new possibility to detect the DM model with pseudoscalar mediators. Second, if m_a is light, the cross section also becomes large because the suppression of the loop functions is weakened. In figure 9, we showed the cross section at the four benchmark points. There are large regions where the cross section is above the neutrino floor while keeping the DM-pseudoscalar coupling perturbative.

The loop corrections in the scattering processes are often crucial. The DM model of winos, the superpartner of $\mathrm{SU}(2)_L$ gauge bosons, is one of the examples [43–45]. In this model, the tree-level contribution is suppressed, and there are box diagrams which induce the SI scattering effects at the loop level. As pointed out in [13], the same situation also happens in inelastic DM models which contain DM candidates with a tiny mass splitting. In these models, the two-loop calculations are necessary to evaluate the cross section and the same technique shown in this paper is available.

Acknowledgments

This work was supported by JSPS KAKENHI Grant Number 16K17715 [T.A.] and by Grant-in-Aid for Scientific research from the Ministry of Education, Science, Sports, and Culture (MEXT), Japan, No. 16H06492 [J.H.]. The work of J.H. is also supported by World Premier International Research Center Initiative (WPI Initiative), MEXT, Japan.

JHEP02(2019)028

A Scalar trilinear couplings

The expressions of the scalar trilinear couplings in eq. (2.19) are as follows :

$$\begin{aligned} g_{haa} =& -\frac{2m_a^2}{v}s_{\beta-\alpha}\sin^2\theta - \frac{m_h^2}{v}\sin^2\theta\frac{s_{\beta-\alpha}t_\beta + c_{\beta-\alpha}(1-t_\beta^2)}{t_\beta} \\ &+ \frac{M^2}{v}\sin^2\theta\frac{2s_{\beta-\alpha}t_\beta + c_{\beta-\alpha}(1-t_\beta^2)}{t_\beta} \\ &- 2c_1 v\cos^2\theta\frac{s_{\beta-\alpha}-c_{\beta-\alpha}t_\beta}{1+t_\beta^2} - 2c_2 v\cos^2\theta\frac{t_\beta(s_{\beta-\alpha}t_\beta + c_{\beta-\alpha})}{1+t_\beta^2}, \end{aligned} \tag{A.1}$$

$$\begin{aligned} g_{haA} =& \frac{m_A^2}{2v}s_{\beta-\alpha}\sin 2\theta + \frac{m_a^2}{2v}s_{\beta-\alpha}\sin 2\theta + \frac{m_h^2}{2v}\sin 2\theta\frac{s_{\beta-\alpha}t_\beta + c_{\beta-\alpha}(1-t_\beta^2)}{t_\beta} \\ &- \frac{M^2}{2v}\sin 2\theta\frac{2s_{\beta-\alpha}t_\beta + c_{\beta-\alpha}(1-t_\beta^2)}{t_\beta} \\ &- c_1 v\sin 2\theta\frac{s_{\beta-\alpha}-c_{\beta-\alpha}t_\beta}{1+t_\beta^2} - c_2 v\sin 2\theta\frac{t_\beta(s_{\beta-\alpha}t_\beta + c_{\beta-\alpha})}{1+t_\beta^2}, \end{aligned} \tag{A.2}$$

$$\begin{aligned} g_{hAA} =& -\frac{2m_A^2}{v}s_{\beta-\alpha}\cos^2\theta - \frac{m_h^2}{v}\cos^2\theta\frac{s_{\beta-\alpha}t_\beta + c_{\beta-\alpha}(1-t_\beta^2)}{t_\beta} \\ &+ \frac{M^2}{v}\cos^2\theta\frac{2s_{\beta-\alpha}t_\beta + c_{\beta-\alpha}(1-t_\beta^2)}{t_\beta} \\ &- 2c_1 v\sin^2\theta\frac{s_{\beta-\alpha}-c_{\beta-\alpha}t_\beta}{1+t_\beta^2} - 2c_2 v\sin^2\theta\frac{t_\beta(s_{\beta-\alpha}t_\beta + c_{\beta-\alpha})}{1+t_\beta^2}, \end{aligned} \tag{A.3}$$

$$\begin{aligned} g_{Haa} =& -\frac{2m_a^2}{v}c_{\beta-\alpha}\sin^2\theta + \frac{m_H^2}{v}\sin^2\theta\frac{s_{\beta-\alpha}(1-t_\beta^2) - c_{\beta-\alpha}t_\beta}{t_\beta} \\ &- \frac{M^2}{v}\sin^2\theta\frac{s_{\beta-\alpha}(1-t_\beta^2) - 2c_{\beta-\alpha}t_\beta}{t_\beta} \\ &- 2c_1 v\cos^2\theta\frac{s_{\beta-\alpha}t_\beta + c_{\beta-\alpha}}{1+t_\beta^2} + 2c_2 v\cos^2\theta\frac{t_\beta(s_{\beta-\alpha}-c_{\beta-\alpha}t_\beta)}{1+t_\beta^2}, \end{aligned} \tag{A.4}$$

$$\begin{aligned} g_{HaA} =& \frac{m_A^2}{2v}c_{\beta-\alpha}\sin 2\theta + \frac{m_a^2}{2v}c_{\beta-\alpha}\sin 2\theta - \frac{m_H^2}{2v}\sin 2\theta\frac{s_{\beta-\alpha}(1-t_\beta^2) - c_{\beta-\alpha}t_\beta}{t_\beta} \\ &+ \frac{M^2}{2v}\sin 2\theta\frac{s_{\beta-\alpha}(1-t_\beta^2) - 2c_{\beta-\alpha}t_\beta}{t_\beta} \\ &- c_1 v\sin 2\theta\frac{s_{\beta-\alpha}t_\beta + c_{\beta-\alpha}}{1+t_\beta^2} + c_2 v\sin 2\theta\frac{t_\beta(s_{\beta-\alpha}-c_{\beta-\alpha}t_\beta)}{1+t_\beta^2}, \end{aligned} \tag{A.5}$$

$$\begin{aligned} g_{HAA} =& -\frac{2m_A^2}{v}c_{\beta-\alpha}\cos^2\theta + \frac{m_H^2}{v}\cos^2\theta\frac{s_{\beta-\alpha}(1-t_\beta^2) + c_{\beta-\alpha}t_\beta}{t_\beta} \\ &- \frac{M^2}{v}\cos^2\theta\frac{s_{\beta-\alpha}(1-t_\beta^2) - 2c_{\beta-\alpha}t_\beta}{t_\beta} \\ &- 2c_1 v\sin^2\theta\frac{s_{\beta-\alpha}t_\beta - c_{\beta-\alpha}}{1+t_\beta^2} + 2c_2 v\sin^2\theta\frac{t_\beta(s_{\beta-\alpha}-c_{\beta-\alpha}t_\beta)}{1+t_\beta^2}, \end{aligned} \tag{A.6}$$

JHEP02(2019)028

where

$$M^2 = \frac{m_3^2}{\sin\beta\cos\beta}, \quad s_{\beta-\alpha} = \sin(\beta-\alpha), \quad c_{\beta-\alpha} = \cos(\beta-\alpha). \tag{A.7}$$

Taking the alignment limit, $\sin(\beta-\alpha) \to 1$, we find

$$g_{haa} = (2M^2 - 2m_a^2 - m_h^2)\frac{\sin^2\theta}{v} - 2v\frac{c_1 + c_2 t_\beta^2}{1+t_\beta^2}\cos^2\theta, \tag{A.8}$$

$$g_{haA} = -(2M^2 - m_a^2 - m_A^2 - m_h^2)\frac{\sin 2\theta}{2v} - v\frac{c_1 + c_2 t_\beta^2}{1+t_\beta^2}\sin 2\theta, \tag{A.9}$$

$$g_{hAA} = (2M^2 - 2m_A^2 - m_h^2)\frac{\cos^2\theta}{v} - 2v\frac{c_1 + c_2 t_\beta^2}{1+t_\beta^2}\sin^2\theta, \tag{A.10}$$

$$g_{Haa} = (M^2 - m_H^2)\frac{\sin^2\theta}{v}\left(1 - \frac{1}{t_\beta}\right) - 2v(c_1 - c_2)\frac{t_\beta}{1+t_\beta^2}\cos^2\theta, \tag{A.11}$$

$$g_{HaA} = (m_H^2 - M^2)\frac{\sin 2\theta}{2v}\left(1 - \frac{1}{t_\beta}\right) - v(c_1 - c_2)\frac{t_\beta}{1+t_\beta^2}\sin 2\theta, \tag{A.12}$$

$$g_{HAA} = (M^2 - m_H^2)\frac{\cos^2\theta}{v}\left(1 - \frac{1}{t_\beta}\right) - 2v(c_1 - c_2)\frac{t_\beta}{1+t_\beta^2}\sin^2\theta. \tag{A.13}$$

In the previous work [11], they set $m_H^2 = m_A^2 = M^2$ and $c_1 = c_2 = 0$. In this case, we find $g_{Ha_ia_j} = 0$ where $a_i = a, A$.

B Details of the calculations of the box diagrams

In the following, we show how to derive the effective operators from the box diagrams.

B.1 The derivation of $C_q^{\rm box}$, $C_q^{(1){\rm box}}$, and $C_q^{(2){\rm box}}$

We show the details of the calculations of $C_q^{\rm box}$, $C_q^{(1){\rm box}}$, and $C_q^{(2){\rm box}}$ shown in section 3.2.1. Note that we calculate the amplitude of the DM-quark scattering process in the zero momentum transfer limit. Summing up the amplitude of the box diagrams shown in figure 10, we obtain

$$\begin{aligned} i\mathcal{M} = &\left(\frac{m_q}{v}\right)^2 \xi^\chi_{a_i}\xi^\chi_{a_j}\xi^q_{a_i}\xi^q_{a_j}\left[\bar{u}_\chi(p_\chi)\gamma^\mu u_\chi(p_\chi)\right]\left[\bar{u}_q(p_q)\gamma^\nu u_q(p_q)\right] \\ &\times \int \frac{d^D\ell}{(2\pi)^D}\frac{\ell_\mu\ell_\nu}{\left[(\ell+p_\chi)^2 - m_\chi^2\right](\ell^2 - m_{a_i}^2)(\ell^2 - m_{a_j}^2)} \\ &\times \left[\frac{-1}{(\ell-p_q)^2 - m_q^2} + \frac{1}{(\ell+p_q)^2 - m_q^2}\right], \end{aligned} \tag{B.1}$$

where $u_\chi(p_\chi)$ is the DM wave function with its momentum p_χ, and $u_q(p_q)$ is the quark wave function with its momentum p_q. We expand the terms in the bracket in eq. (B.1) by the quark momentum and keep the leading term as follows:

$$\frac{-1}{(\ell-p_q)^2 - m_q^2} + \frac{1}{(\ell+p_q)^2 - m_q^2} = -\frac{4\ell\cdot p_q}{\ell^4} + \mathcal{O}(p_q^2). \tag{B.2}$$

JHEP02(2019)028

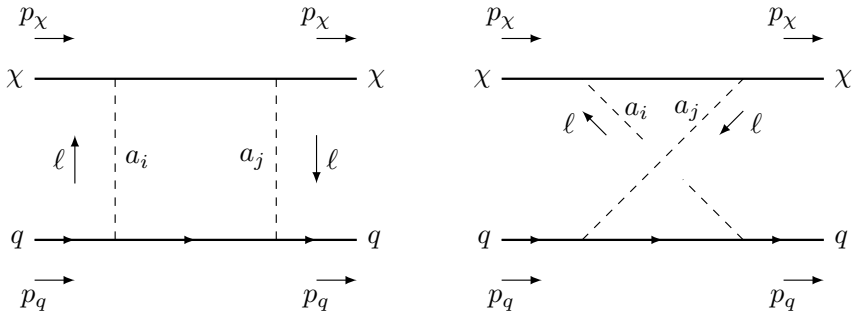

Figure 10. The box diagrams and their momentum assignments.

Here we have used $p_q^2 = m_q^2$. After this expansion, the amplitude of these diagrams is

$$\begin{aligned} i\mathcal{M} = {} & iA_1 m_\chi m_q \Big[\bar{u}_\chi(p_\chi)u_\chi(p_\chi)\Big]\Big[\bar{u}_q(p_q)u_q(p_q)\Big] \\ & + iA_1(p_\chi\cdot p_q)\Big[\bar{u}_\chi(p_\chi)\gamma^\mu u_\chi(p_\chi)\Big]\Big[\bar{u}_q(p_q)\gamma_\mu u_q(p_q)\Big] \\ & + iA_1\Big[\bar{u}_\chi(p_\chi)\not{p}_q u_\chi(p_\chi)\Big]\Big[\bar{u}_q(p_q)\not{p}_\chi u_q(p_q)\Big] \\ & + iA_2 m_\chi(p_\chi\cdot p_q)\Big[\bar{u}_\chi(p_\chi)u_\chi(p_\chi)\Big]\Big[\bar{u}_q(p_q)\not{p}_\chi u_q(p_q)\Big], \end{aligned} \tag{B.3}$$

where

$$\begin{aligned} A_1 = \frac{-4}{(4\pi)^2}\left(\frac{m_q}{v}\right)^2 \times \Bigg\{ & \frac{(\xi_a^\chi \xi_a^q)^2}{m_a^2}\left[X_{001}(p^2,m_\chi^2,0,m_a^2) - X_{001}(p^2,m_\chi^2,m_a^2,0)\right] \\ & + \frac{(\xi_A^\chi \xi_A^q)^2}{m_A^2}\left[X_{001}(p^2,m_\chi^2,0,m_A^2) - X_{001}(p^2,m_\chi^2,m_A^2,0)\right] \\ & + 2\frac{\xi_A^\chi \xi_a^\chi \xi_A^q \xi_a^q}{m_A^2 - m_a^2}\left[X_{001}(p^2,m_\chi^2,m_A^2,0) - X_{001}(p^2,m_\chi^2,m_a^2,0)\right]\Bigg\}, \end{aligned} \tag{B.4}$$

$$\begin{aligned} A_2 = \frac{-4}{(4\pi)^2}\left(\frac{m_q}{v}\right)^2 \times \Bigg\{ & \frac{(\xi_a^\chi \xi_a^q)^2}{m_a^2}\left[X_{111}(p^2,m_\chi^2,0,m_a^2) - X_{111}(p^2,m_\chi^2,m_a^2,0)\right] \\ & + \frac{(\xi_A^\chi \xi_A^q)^2}{m_A^2}\left[X_{111}(p^2,m_\chi^2,0,m_A^2) - X_{111}(p^2,m_\chi^2,m_A^2,0)\right] \\ & + 2\frac{\xi_A^\chi \xi_a^\chi \xi_A^q \xi_a^q}{m_A^2 - m_a^2}\left[X_{111}(p^2,m_\chi^2,m_A^2,0) - X_{111}(p^2,m_\chi^2,m_a^2,0)\right]\Bigg\}. \end{aligned} \tag{B.5}$$

Loop functions X_{001} and X_{111} are defined in appendix C.2. From this amplitude, we find the following effective operators.

$$\begin{aligned} \mathcal{L}_{\text{eff}} = {} & \frac{1}{2}(m_\chi A_1) m_q \bar{\chi}\chi\bar{q}q + \frac{1}{2}A_1(\bar{\chi}i\partial^\mu\gamma^\nu\chi)(\bar{q}i\partial_\mu\gamma_\nu q) + \frac{1}{2}A_1(\bar{\chi}i\partial^\mu\gamma^\nu\chi)(\bar{q}i\partial_\nu\gamma_\mu q) \\ & + \frac{1}{2}(m_\chi A_2)(\bar{\chi}i\partial^\mu i\partial^\nu\chi)(\bar{q}i\partial_\mu\gamma_\nu q). \end{aligned} \tag{B.6}$$

JHEP02(2019)028

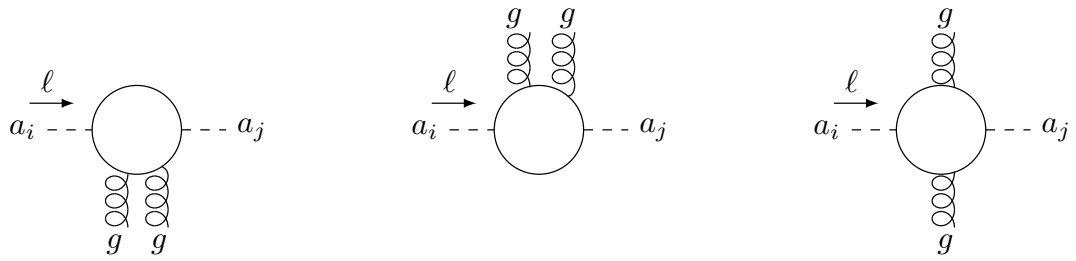

Figure 11. The diagrams which contribute to the effective operators $a_i a_j G^a_{\mu\nu} G^{a\mu\nu}$, where $a_i = a, A$.

Then, we perform the irreducible decomposition to these operators.

$$\begin{aligned}\bar{q} i\partial^\mu \gamma^\nu q &= \bar{q}\left[\frac{i\partial^\mu\gamma^\nu + i\partial^\nu\gamma^\mu}{2} - \frac{1}{4}g^{\mu\nu} i\not{\partial}\right] q + \bar{q}\left[\frac{i\partial^\mu\gamma^\nu - i\partial^\nu\gamma^\mu}{2}\right] q + \frac{1}{4}g^{\mu\nu}\bar{q} i\not{\partial} q \\ &= \mathcal{O}^q_{\mu\nu} + \frac{1}{4}g^{\mu\nu} m_q \bar{q} q. \end{aligned} \tag{B.7}$$

Note that we drop the anti-symmetric term in the last line because it does not contribute to the nucleon matrix element. The last term in eq. (B.7) gives the contribution to the scalar operator $\bar{\chi}\chi\bar{q}q$. After this decomposition, we find

$$\mathcal{L}_{\text{eff}} = \frac{1}{2} C_q^{\text{box}} m_q \bar{\chi}\chi\bar{q}q + \frac{1}{2} C_q^{(1)\text{box}} \bar{\chi} i\partial^\mu \gamma^\nu \chi \mathcal{O}^q_{\mu\nu} + \frac{1}{2} C_q^{(2)\text{box}} \bar{\chi} i\partial^\mu i\partial^\nu \chi \mathcal{O}^q_{\mu\nu}, \tag{B.8}$$

where

$$C_q^{\text{box}} = \frac{m_\chi}{4}\left(6A_1 + m_\chi^2 A_2\right), \tag{B.9}$$

$$C_q^{(1)\text{box}} = 2A_1, \tag{B.10}$$

$$C_q^{(2)\text{box}} = m_\chi A_2. \tag{B.11}$$

These coefficients correspond to the Wilson coefficients in eqs. (3.19)–(3.21).

B.2 The derivation of C_G^{box}

We show the details of the derivation of C_G^{box} shown in section 3.2.2.

First, we calculate the heavy quark loops in the two-loop diagrams. In figure 11, we show the pseudoscalar-gluon scattering diagrams. We calculate the amplitude of these diagrams in the gluon background field theory. We use the Fock-Schwinger gauge for the gluon field. The amplitude with the external pseudoscalar momentum ℓ is as follows:

$$i\mathcal{M} = i\Pi_{a_i a_j}(\ell^2)\left[G^a_{\mu\nu} G^{a\mu\nu}\right], \tag{B.12}$$

where

$$\begin{aligned}\Pi_{a_i a_j}(\ell^2) = \frac{\alpha_s}{24\pi}\left[G^a_{\mu\nu} G^{a\mu\nu}\right] \sum_{Q=c,b,t}\left(\frac{m_Q}{v}\right)^2 \xi^Q_{a_i}\xi^Q_{a_j} \\ \times \int_0^1 dx \left[\frac{3x(1-x)}{[m_Q^2 - x(1-x)\ell^2]} + \frac{m_Q^2\cdot(2+5x-5x^2)}{[m_Q^2 - x(1-x)\ell^2]^2} - \frac{2m_Q^4(1-2x+2x^2)}{[m_Q^2 - x(1-x)\ell^2]^3}\right].\end{aligned} \tag{B.13}$$

Note that the gluon in eq. (B.12) is the external field.

JHEP02(2019)028

Next, we read out the effective operator $a_i a_j G^a_{\mu\nu} G^{a\mu\nu}$ from eq. (B.12) and calculate the amplitude of the two-loop diagrams shown in figure 3. The amplitude can be expressed using $\Pi_{a_i a_j}(\ell^2)$ as follows:

$$i\mathcal{M} = \sum_{a_i=a,A} (-\xi^\chi_{a_i}\xi^\chi_{a_j}) \left[\overline{u}_\chi(p_\chi)\gamma^\rho u_\chi(p_\chi)\right]\left[G^a_{\mu\nu}G^{a\mu\nu}\right] \times \int \frac{d^D\ell}{(2\pi)^D} \frac{\ell_\rho}{[(\ell+p_\chi)^2-m_\chi^2](\ell^2-m_{a_i}^2)(\ell^2-m_{a_j}^2)} \Pi_{a_i a_j}(\ell^2). \tag{B.14}$$

Reading out the effective operator from this amplitude, we obtain $C_G^{\rm box}$ in eq. (3.24).

C Loop functions

In the following, we show the expressions of the loop functions used in section 3. For the later convenience, we define $\tilde{\epsilon}$ as follows:

$$\frac{2}{\tilde{\epsilon}} = \frac{2}{\epsilon} - \gamma_E + \log(4\pi), \tag{C.1}$$

where $\epsilon = 4 - D$ and γ_E is the Euler-Mascheroni constant.

C.1 *B* functions

We show the definitions of B functions $(B_0, B_1, B_{00}, B_{11}, B_{001}, B_{111})$ which are the same as those in `LoopTools` [42].

$$\int \frac{d^D\ell}{(2\pi)^D} \frac{1}{(\ell^2-m^2)[(\ell+p)^2-M^2]} = \frac{i}{(4\pi)^2} B_0(p^2,m^2,M^2), \tag{C.2}$$

$$\int \frac{d^D\ell}{(2\pi)^D} \frac{\ell_\mu}{(\ell^2-m^2)[(\ell+p)^2-M^2]} = \frac{i}{(4\pi)^2} p_\mu B_1(p^2,m^2,M^2), \tag{C.3}$$

$$\int \frac{d^D\ell}{(2\pi)^D} \frac{\ell_\mu\ell_\nu}{(\ell^2-m^2)[(\ell+p)^2-M^2]} = \frac{i}{(4\pi)^2}\left[g_{\mu\nu}B_{00}(p^2,m^2,M^2)+p_\mu p_\nu B_{11}(p^2,m^2,M^2)\right], \tag{C.4}$$

$$\int \frac{d^D\ell}{(2\pi)^D} \frac{\ell_\mu\ell_\nu\ell_\rho}{(\ell^2-m^2)[(\ell+p)^2-M^2]} = \frac{i}{(4\pi)^2}\Big[(g_{\mu\nu}p_\rho+g_{\nu\rho}p_\mu+g_{\rho\mu}p_\nu)B_{001}(p^2,m^2,M^2)+p_\mu p_\nu p_\rho B_{111}(p^2,m^2,M^2)\Big]. \tag{C.5}$$

The expressions of the B functions are

$$B_0(p^2,m^2,M^2) = \int_0^1 dx \left[\frac{2}{\tilde{\epsilon}} + \log\left(\frac{\mu^2}{m^2x+M^2(1-x)-p^2x(1-x)}\right)\right], \tag{C.6}$$

$$B_1(p^2,m^2,M^2) = \int_0^1 dx[-(1-x)] \left[\frac{2}{\tilde{\epsilon}} + \log\left(\frac{\mu^2}{m^2x+M^2(1-x)-p^2x(1-x)}\right)\right], \tag{C.7}$$

JHEP02(2019)028

$$B_{00}(p^2,m^2,M^2)=\int_0^1 dx\frac{m^2x+M^2(1-x)-p^2x(1-x)}{2}\times\left[\frac{2}{\tilde{\epsilon}}+1+\log\left(\frac{\mu^2}{m^2x+M^2(1-x)-p^2x(1-x)}\right)\right], \tag{C.8}$$

$$B_{11}(p^2,m^2,M^2)=\int_0^1 dx(1-x)^2\left[\frac{2}{\tilde{\epsilon}}+\log\left(\frac{\mu^2}{m^2x+M^2(1-x)-p^2x(1-x)}\right)\right], \tag{C.9}$$

$$B_{001}(p^2,m^2,M^2)=\int_0^1 dx\frac{-(1-x)[m^2x+M^2(1-x)-p^2x(1-x)]}{2}\times\left[\frac{2}{\tilde{\epsilon}}+1+\log\left(\frac{\mu^2}{m^2x+M^2(1-x)-p^2x(1-x)}\right)\right], \tag{C.10}$$

$$B_{111}(p^2,m^2,M^2)=\int_0^1 dx[-(1-x)^3]\left[\frac{2}{\tilde{\epsilon}}+\log\left(\frac{\mu^2}{m^2x+M^2(1-x)-p^2x(1-x)}\right)\right]. \tag{C.11}$$

The derivative of B_0 with respect to p^2 are

$$\frac{\partial}{\partial p^2}B_0(p^2,m^2,M^2)=\int_0^1 dx\frac{x(1-x)}{m^2x+M^2(1-x)-p^2x(1-x)}. \tag{C.12}$$

C.2 *X* functions

The definitions of X functions (X_{001},X_{111}) are as follows:

$$\begin{aligned}&\int\frac{d^D\ell}{(2\pi)^D}\frac{\ell_\mu\ell_\nu\ell_\rho}{[(\ell+p)^2-M^2]\,(\ell^2-m_1^2)^2(\ell^2-m_2^2)} \\ &=\frac{i}{(4\pi)^2}\Big[(g_{\mu\nu}p_\rho+g_{\nu\rho}p_\mu+g_{\rho\mu}p_\nu)X_{001}(p^2,M^2,m_1^2,m_2^2)+p_\mu p_\nu p_\rho X_{111}(p^2,M^2,m_1^2,m_2^2)\Big].\end{aligned} \tag{C.13}$$

X functions can be expressed using Feynman parameter integrals, and using B functions.

$$\begin{aligned}X_{001}(p^2,M^2,m_1^2,m_2^2)&=\int_0^1 dx\int_0^{1-x}dy\frac{\frac{1}{2}x(1-x-y)}{M^2x+m_1^2y+m_2^2(1-x-y)-p^2x(1-x)} \\ &=\frac{1}{(m_1^2-m_2^2)^2}\left[B_{001}(p^2,m_1^2,M^2)-B_{001}(p^2,m_2^2,M^2)\right] \\ &\quad-\frac{1}{m_1^2-m_2^2}\left[\frac{\partial}{\partial p^2}B_{00}(p^2,m_2^2,M^2)\right],\end{aligned} \tag{C.14}$$

$$\begin{aligned}X_{111}(p^2,M^2,m_1^2,m_2^2)&=\int_0^1 dx\int_0^{1-x}dy\frac{-x^3(1-x-y)}{[M^2x+m_1^2y+m_2^2(1-x-y)-p^2x(1-x)]^2} \\ &=\frac{1}{(m_1^2-m_2^2)^2}\left[B_{111}(p^2,m_1^2,M^2)-B_{111}(p^2,m_2^2,M^2)\right] \\ &\quad-\frac{1}{m_1^2-m_2^2}\frac{\partial}{\partial p^2}B_{11}(p^2,m_2^2,M^2).\end{aligned} \tag{C.15}$$

JHEP02(2019)028

C.3 Y functions

The definitions of Y functions (Y_1, Y_2, Y_3) are as follows:

$$\int \frac{d^D\ell}{(2\pi)^D} \frac{\ell_\mu}{[(\ell+p)^2-m_\chi^2](\ell^2-m_A^2)\left[\ell^2-\frac{m_q^2}{x(1-x)}\right]} = \frac{i}{(4\pi)^2} p_\mu Y_1(p^2, m_\chi^2, m_A^2, m_q^2), \quad \text{(C.16)}$$

$$\int \frac{d^D\ell}{(2\pi)^D} \frac{\ell_\mu}{[(\ell+p)^2-m_\chi^2](\ell^2-m_A^2)\left[\ell^2-\frac{m_q^2}{x(1-x)}\right]^2} = \frac{i}{(4\pi)^2} p_\mu Y_2(p^2, m_\chi^2, m_A^2, m_q^2), \quad \text{(C.17)}$$

$$\int \frac{d^D\ell}{(2\pi)^D} \frac{\ell_\mu}{[(\ell+p)^2-m_\chi^2](\ell^2-m_A^2)\left[\ell^2-\frac{m_q^2}{x(1-x)}\right]^3} = \frac{i}{(4\pi)^2} p_\mu Y_3(p^2, m_\chi^2, m_A^2, m_q^2). \quad \text{(C.18)}$$

Y functions can be expressed using Feynman parameter integrals, and using B, C, D functions.

$$\begin{aligned} Y_1(m_\chi^2, m_\chi^2, m_A^2, m_q^2) &= \int_0^1 dy \int_0^{1-y} dz \frac{-2y}{\left[m_\chi^2 y^2 + \frac{m_q^2}{x(1-x)} z + m_A^2(1-y-z)\right]} \\ &= \frac{1}{m_A^2 - \frac{m_q^2}{x(1-x)}} \left[B_1(m_\chi^2, m_A^2, m_\chi^2) - B_1(m_\chi^2, \tfrac{m_q^2}{x(1-x)}, m_\chi^2)\right], \end{aligned} \quad \text{(C.19)}$$

$$\begin{aligned} Y_2(m_\chi^2, m_\chi^2, m_A^2, m_q^2) &= \int_0^1 dy \int_0^{1-y} dz \frac{2yz}{\left[m_\chi^2 y^2 + \frac{m_q^2}{x(1-x)} z + m_A^2(1-y-z)\right]^2} \\ &= \frac{1}{m_A^2 - \frac{m_q^2}{x(1-x)}} \left[Y_1(m_\chi^2, m_\chi^2, m_A^2, m_q^2) - C_2(m_\chi^2, \tfrac{m_q^2}{x(1-x)}, m_\chi^2)\right], \end{aligned} \quad \text{(C.20)}$$

$$\begin{aligned} Y_3(m_\chi^2, m_\chi^2, m_A^2, m_q^2) &= \int_0^1 dy \int_0^{1-y} dz \frac{-4yz^2}{\left[m_\chi^2 y^2 + \frac{m_q^2}{x(1-x)} z + m_A^2(1-y-z)\right]^3} \\ &= \frac{1}{m_A^2 - \frac{m_q^2}{x(1-x)}} \left[Y_2(m_\chi^2, m_\chi^2, m_A^2, m_q^2) - D_3\left(0, 0, m_\chi^2, m_\chi^2, \tfrac{m_q^2}{x(1-x)}, \tfrac{m_q^2}{x(1-x)}, \tfrac{m_q^2}{x(1-x)}, m_\chi^2\right)\right]. \end{aligned} \quad \text{(C.21)}$$

The definitions of C_2, D_3 are in appendix C.4.

C.4 C_2, D_3 functions

The definitions of C_2 and D_3 functions are as follows:

$$\int \frac{d^D\ell}{(2\pi)^D} \frac{\ell_\mu}{(\ell^2-m^2)^2[(\ell+p)^2-M^2]} = \frac{i}{(4\pi)^2} p_\mu C_2(p^2, m^2, M^2), \quad \text{(C.22)}$$

$$\int \frac{d^D\ell}{(2\pi)^D} \frac{\ell_\mu}{(\ell^2-m^2)^3[(\ell+p)^2-M^2]} = \frac{i}{(4\pi)^2} p_\mu D_3(p^2, m^2, M^2). \quad \text{(C.23)}$$

JHEP02(2019)028

We have some variations to express C_2, D_3 functions [40].

$$C_2(p^2,m^2,M^2) = \int_0^1 dx \frac{x(1-x)}{m^2x+M^2x-p^2x(1-x)} = \frac{\partial}{\partial p^2} B_0(p^2,m^2,M^2), \tag{C.24}$$

$$\begin{aligned} D_3(p^2,m^2,M^2) &= \int_0^1 dx \frac{-\frac{1}{2}x^2(1-x)}{[m^2x+M^2x-p^2x(1-x)]^2} \\ &= \frac{1}{2}\frac{\partial}{\partial m^2}\frac{\partial}{\partial p^2} B_0(p^2,m^2,M^2) \\ &= \frac{1}{2}\left(\frac{\partial}{\partial m^2}\right)^2 B_0(p^2,m^2,M^2) \\ &= \frac{-p^2+m^2+M^2}{(p^4+m^4+M^4-2p^2m^2-2p^2M^2-2m^2M^2)^2} \\ &\quad \times \left[(M^2-m^2+p^2)\left[-B_0(p^2,m^2,M^2)+B_0(0,m^2,m^2)+2\right]-2M^2\log\frac{M^2}{m^2}\right] \\ &\quad + \frac{1}{2}\frac{1}{(p^4+m^4+M^4-2p^2m^2-2p^2M^2-2m^2M^2)} \\ &\quad \times \left[-B_0(p^2,m^2,M^2)+B_0(0,m^2,m^2)+2-(p^2-m^2-M^2)\frac{\partial}{\partial p^2}B_0(p^2,m^2,M^2)\right]. \end{aligned} \tag{C.25}$$

C.5 $\partial F(m_a^2)/\partial m_a^2$ in loop functions

$\partial Y_n(p^2,m_\chi^2,m_a^2,m_q^2)/\partial m_a^2$ $(n=1,2,3)$ can be expressed in the loop functions introduced above.

$$\frac{\partial}{\partial m_a^2} Y_1(p^2,m_\chi^2,m_a^2,m_q^2) = \frac{1}{m_a^2-\frac{m_q^2}{x(1-x)}}\left[\frac{\partial}{\partial m_\chi^2}B_0(m_\chi^2,m_a^2,m_\chi^2) - Y_1(p^2,m_\chi^2,m_a^2,m_q^2)\right], \tag{C.26}$$

$$\frac{\partial}{\partial m_a^2} Y_2(p^2,m_\chi^2,m_a^2,m_q^2) = \frac{1}{m_a^2-\frac{m_q^2}{x(1-x)}}\left[\frac{\partial}{\partial m_a^2}Y_1(p^2,m_\chi^2,m_a^2,m_q^2) - Y_2(p^2,m_\chi^2,m_a^2,m_q^2)\right], \tag{C.27}$$

$$\frac{\partial}{\partial m_a^2} Y_3(p^2,m_\chi^2,m_a^2,m_q^2) = \frac{1}{m_a^2-\frac{m_q^2}{x(1-x)}}\left[\frac{\partial}{\partial m_a^2}Y_2(p^2,m_\chi^2,m_a^2,m_q^2) - Y_3(p^2,m_\chi^2,m_a^2,m_q^2)\right]. \tag{C.28}$$

The expression for $\partial F(m_a^2)/\partial m_a^2$ using the loop functions is

$$\begin{aligned} \frac{\partial F(m_a^2)}{\partial m_a^2} = \int_0^1 dx \Big\{ & 3\frac{\partial}{\partial m_a^2}Y_1(p^2,m_\chi^2,m_a^2,m_q^2) \\ & - m_q^2\frac{(2+5x-5x^2)}{x^2(1-x)^2}\frac{\partial}{\partial m_a^2}Y_2(p^2,m_\chi^2,m_a^2,m_q^2) \\ & - 2m_q^4\frac{(1-2x+2x^2)}{x^3(1-x)^3}\frac{\partial}{\partial m_a^2}Y_3(p^2,m_\chi^2,m_a^2,m_q^2)\Big\}. \end{aligned} \tag{C.29}$$

JHEP02(2019)028

References

[1] LUX collaboration, *Limits on spin-dependent WIMP-nucleon cross section obtained from the complete LUX exposure*, *Phys. Rev. Lett.* **118** (2017) 251302 [arXiv:1705.03380] [INSPIRE].

[2] PandaX-II collaboration, *Dark Matter Results From 54-Ton-Day Exposure of PandaX-II Experiment*, *Phys. Rev. Lett.* **119** (2017) 181302 [arXiv:1708.06917] [INSPIRE].

[3] XENON collaboration, *Dark Matter Search Results from a One Ton-Year Exposure of XENON1T*, *Phys. Rev. Lett.* **121** (2018) 111302 [arXiv:1805.12562] [INSPIRE].

[4] M. Escudero, A. Berlin, D. Hooper and M.-X. Lin, *Toward (Finally!) Ruling Out Z and Higgs Mediated Dark Matter Models*, *JCAP* **12** (2016) 029 [arXiv:1609.09079] [INSPIRE].

[5] M. Escudero, D. Hooper and S.J. Witte, *Updated Collider and Direct Detection Constraints on Dark Matter Models for the Galactic Center Gamma-Ray Excess*, *JCAP* **02** (2017) 038 [arXiv:1612.06462] [INSPIRE].

[6] S. Ipek, D. McKeen and A.E. Nelson, *A Renormalizable Model for the Galactic Center Gamma Ray Excess from Dark Matter Annihilation*, *Phys. Rev.* **D 90** (2014) 055021 [arXiv:1404.3716] [INSPIRE].

[7] J.M. No, *Looking through the pseudoscalar portal into dark matter: Novel mono-Higgs and mono-Z signatures at the LHC*, *Phys. Rev.* **D 93** (2016) 031701 [arXiv:1509.01110] [INSPIRE].

[8] D. Goncalves, P.A.N. Machado and J.M. No, *Simplified Models for Dark Matter Face their Consistent Completions*, *Phys. Rev.* **D 95** (2017) 055027 [arXiv:1611.04593] [INSPIRE].

[9] M. Bauer, U. Haisch and F. Kahlhoefer, *Simplified dark matter models with two Higgs doublets: I. Pseudoscalar mediators*, *JHEP* **05** (2017) 138 [arXiv:1701.07427] [INSPIRE].

[10] P. Tunney, J.M. No and M. Fairbairn, *Probing the pseudoscalar portal to dark matter via $\bar{b}bZ(\to \ell\ell)+ \not{E}_T$: From the LHC to the Galactic Center excess*, *Phys. Rev.* **D 96** (2017) 095020 [arXiv:1705.09670] [INSPIRE].

[11] G. Arcadi, M. Lindner, F.S. Queiroz, W. Rodejohann and S. Vogl, *Pseudoscalar Mediators: A WIMP model at the Neutrino Floor*, *JCAP* **03** (2018) 042 [arXiv:1711.02110] [INSPIRE].

[12] P. Pani and G. Polesello, *Dark matter production in association with a single top-quark at the LHC in a two-Higgs-doublet model with a pseudoscalar mediator*, *Phys. Dark Univ.* **21** (2018) 8 [arXiv:1712.03874] [INSPIRE].

[13] N.F. Bell, G. Busoni and I.W. Sanderson, *Loop Effects in Direct Detection*, *JCAP* **08** (2018) 017 [*Erratum ibid.* **01** (2019) E01] [arXiv:1803.01574] [INSPIRE].

[14] T. Li, *Revisiting the direct detection of dark matter in simplified models*, *Phys. Lett.* **B 782** (2018) 497 [arXiv:1804.02120] [INSPIRE].

[15] K. Ghorbani, *Fermionic dark matter with pseudo-scalar Yukawa interaction*, *JCAP* **01** (2015) 015 [arXiv:1408.4929] [INSPIRE].

[16] T. Abe, R. Kitano and R. Sato, *Discrimination of dark matter models in future experiments*, *Phys. Rev.* **D 91** (2015) 095004 [*Erratum ibid.* **D 96** (2017) 019902] [arXiv:1411.1335] [INSPIRE].

[17] S. Baek, P. Ko and J. Li, *Minimal renormalizable simplified dark matter model with a pseudoscalar mediator*, *Phys. Rev.* **D 95** (2017) 075011 [arXiv:1701.04131] [INSPIRE].

JHEP02(2019)028

[18] T. Abe, *Effect of CP-violation in the singlet-doublet dark matter model*, *Phys. Lett.* **B 771** (2017) 125 [arXiv:1702.07236] [INSPIRE].

[19] J. Billard, L. Strigari and E. Figueroa-Feliciano, *Implication of neutrino backgrounds on the reach of next generation dark matter direct detection experiments*, *Phys. Rev.* **D 89** (2014) 023524 [arXiv:1307.5458] [INSPIRE].

[20] XENON collaboration, *Physics reach of the XENON1T dark matter experiment*, *JCAP* **04** (2016) 027 [arXiv:1512.07501] [INSPIRE].

[21] LUX and LZ collaborations, *The Present and Future of Searching for Dark Matter with LUX and LZ*, PoS(ICHEP2016)220 (2016) [arXiv:1611.05525] [INSPIRE].

[22] DARWIN collaboration, *DARWIN: towards the ultimate dark matter detector*, *JCAP* **11** (2016) 017 [arXiv:1606.07001] [INSPIRE].

[23] M.A. Shifman, A.I. Vainshtein and V.I. Zakharov, *Remarks on Higgs Boson Interactions with Nucleons*, *Phys. Lett.* **78B** (1978) 443 [INSPIRE].

[24] V.D. Barger, J.L. Hewett and R.J.N. Phillips, *New Constraints on the Charged Higgs Sector in Two Higgs Doublet Models*, *Phys. Rev.* **D 41** (1990) 3421 [INSPIRE].

[25] Y. Grossman, *Phenomenology of models with more than two Higgs doublets*, *Nucl. Phys.* **B 426** (1994) 355 [hep-ph/9401311] [INSPIRE].

[26] M. Aoki, S. Kanemura, K. Tsumura and K. Yagyu, *Models of Yukawa interaction in the two Higgs doublet model and their collider phenomenology*, *Phys. Rev.* **D 80** (2009) 015017 [arXiv:0902.4665] [INSPIRE].

[27] S.L. Glashow and S. Weinberg, *Natural Conservation Laws for Neutral Currents*, *Phys. Rev.* **D 15** (1977) 1958 [INSPIRE].

[28] X. Liu, L. Bian, X.-Q. Li and J. Shu, *Type-III two Higgs doublet model plus a pseudoscalar confronted with $h \to \mu\tau$, muon $g-2$ and dark matter*, *Nucl. Phys.* **B 909** (2016) 507 [arXiv:1508.05716] [INSPIRE].

[29] ATLAS collaboration, *Combined measurements of Higgs boson production and decay using up to 80 fb^{-1} of proton-proton collision data at $\sqrt{s} = 13$ TeV collected with the ATLAS experiment*, ATLAS-CONF-2018-031 [INSPIRE].

[30] CMS collaboration, *Combined measurements of Higgs boson couplings in proton-proton collisions at $\sqrt{s} = 13$ TeV*, arXiv:1809.10733 [INSPIRE].

[31] M. Misiak and M. Steinhauser, *Weak radiative decays of the B meson and bounds on $M_{H^\pm}$ in the Two-Higgs-Doublet Model*, *Eur. Phys. J.* **C 77** (2017) 201 [arXiv:1702.04571] [INSPIRE].

[32] ATLAS collaboration, *Search for heavy resonances decaying into a W or Z boson and a Higgs boson in final states with leptons and b-jets in 36 fb^{-1} of $\sqrt{s} = 13$ TeV pp collisions with the ATLAS detector*, *JHEP* **03** (2018) 174 [*Erratum ibid.* **11** (2018) 051] [arXiv:1712.06518] [INSPIRE].

[33] CMS collaboration, *Search for a heavy pseudoscalar boson decaying to a Z boson and a Higgs boson at $\sqrt{s} = 13$ TeV*, CMS-PAS-HIG-18-005 [INSPIRE].

[34] CMS collaboration, *Combined measurements of the Higgs boson's couplings at $\sqrt{s} = 13$ TeV*, CMS-PAS-HIG-17-031 [INSPIRE].

[35] J. Hisano, *Effective theory approach to direct detection of dark matter*, arXiv:1712.02947 [INSPIRE].

JHEP02(2019)028

[36] G. Bélanger, F. Boudjema, A. Pukhov and A. Semenov, *MicrOMEGAs$_3$: A program for calculating dark matter observables*, *Comput. Phys. Commun.* **185** (2014) 960 [arXiv:1305.0237] [INSPIRE].

[37] J. Pumplin, D.R. Stump, J. Huston, H.L. Lai, P.M. Nadolsky and W.K. Tung, *New generation of parton distributions with uncertainties from global QCD analysis*, *JHEP* **07** (2002) 012 [hep-ph/0201195] [INSPIRE].

[38] V.A. Novikov, M.A. Shifman, A.I. Vainshtein and V.I. Zakharov, *Calculations in External Fields in Quantum Chromodynamics. Technical Review*, *Fortsch. Phys.* **32** (1984) 585 [INSPIRE].

[39] J. Hisano, K. Ishiwata and N. Nagata, *Gluon contribution to the dark matter direct detection*, *Phys. Rev.* **D 82** (2010) 115007 [arXiv:1007.2601] [INSPIRE].

[40] T. Abe and R. Sato, *Quantum corrections to the spin-independent cross section of the inert doublet dark matter*, *JHEP* **03** (2015) 109 [arXiv:1501.04161] [INSPIRE].

[41] PLANCK collaboration, *Planck 2015 results. XIII. Cosmological parameters*, *Astron. Astrophys.* **594** (2016) A13 [arXiv:1502.01589] [INSPIRE].

[42] T. Hahn and M. Pérez-Victoria, *Automatized one loop calculations in four-dimensions and D-dimensions*, *Comput. Phys. Commun.* **118** (1999) 153 [hep-ph/9807565] [INSPIRE].

[43] J. Hisano, S. Matsumoto, M.M. Nojiri and O. Saito, *Direct detection of the Wino and Higgsino-like neutralino dark matters at one-loop level*, *Phys. Rev.* **D 71** (2005) 015007 [hep-ph/0407168] [INSPIRE].

[44] J. Hisano, K. Ishiwata and N. Nagata, *A complete calculation for direct detection of Wino dark matter*, *Phys. Lett.* **B 690** (2010) 311 [arXiv:1004.4090] [INSPIRE].

[45] J. Hisano, K. Ishiwata and N. Nagata, *QCD Effects on Direct Detection of Wino Dark Matter*, *JHEP* **06** (2015) 097 [arXiv:1504.00915] [INSPIRE].

JHEP02(2019)028